SUPPORTING MATERIAL

Kinetics and Mechanisms of Oxidative Cleavage of HIV RRE RNA by Rev-Coupled Transition Metal Chelates

Jeff C. Joyner,[1,2] Kevin D. Keuper, [1] and J. A. Cowan[1,2,3]*

Contribution from [1] Evans Laboratory of Chemistry, Ohio State University, 100 West 18th Avenue, Columbus, Ohio 43210; [2] The Ohio State Biochemistry Program, 784 Biological Sciences 484 W. 12th Avenue, Columbus, Ohio 43210; and [3] MetalloPharm LLC, 1790 Riverstone Drive, Delaware, OH 43015

Table of Contents for Supporting Information

MATERIALS AND METHODS

Chemicals and Reagents. The custom RNA constructs RRE, with sequence GGU CUG GGC GCA GCG CAA GCU GAC GGU ACA GGC C-3', Fl-RRE, with sequence 5'-Fluorescein-UUG GUC UGG GCG CAG CGC AAG CUG ACG GUA CAG GCC-3', Fl-IRESSLIV, with sequence 5'-Fluorescein-GGA CCG UGC ACC AUG AGC ACG AAU CC-3', and AP-RRE, with sequence 5'-GGU CUG GGC GCA GCG CAA GCU GAC GG(2-AP) ACA GGC C-3' were purchased from Dharmacon. The custom RNA construct Fl-5mer, with sequence 5'-Fluorescein (T)-UGUG-3', was purchased from Integrated DNA Technologies. The peptides GGH-Rev with sequence GGHTRQARRNRRRRWRERQR-NH_2 and KGHK-Rev with sequence KGHKTRQARRNRRRRWRERQR-NH_2 were purchased from Genemed Synthesis Inc. The tripeptide GGH (GGH) and tetrapeptide KGHK (KGHK) were obtained from Bachem. The metal-chelate-Rev species containing combinations of Fe, Co, Ni, and Cu with the chelators DOTA-Rev, DTPA-Rev, EDTA-Rev, NTA-Rev, GGH-Rev, and KGHK-Rev were synthesized as described previously.[1] RNA and peptide species were immediately aliquoted into single-use containers and stored at -80 °C to minimize freeze-thaw cycles. The Fe(II) sulfate heptahydrate, Co(II) chloride hexahydrate, Ni(II) acetate tetrahydrate, and Cu(II) chloride dihydrate salts were purchased from ACROS, J.T.Baker, Aldrich, and J. T. Baker, respectively. Sodium chloride and sodium hydroxide were purchased from Fisher, and HEPES was purchased from Sigma. C_{18} zip-tips and acetonitrile were obtained from Millipore from Fisher, respectively. Matrix components ammonium citrate and 3-hydroxypicolinic acid were obtained from Aldrich and Sigma-Aldrich, respectively. Compound 2-hydroxypropanedial was purchased from Santa Cruz Biotechnology, Inc.

RNA Cleavage Reactions. Reactions of 10 μM catalyst, 1 mM co-reactants (ascorbate, H_2O_2, and/or no co-reactants), and 10 μM RNA were conducted at 37 °C in separate tubes, each containing 20 μL total reaction volume. A reaction buffer consisting of 20 mM HEPES, 100 mM NaCl, pH 7.4 was used in all experiments. Prior to reaction, RNA was heated to 90 °C for 5 min and allowed to cool to 37 °C, and the RNA was immediately added to each pre-incubated tube. For time-dependent reactions, one tube corresponded to one time point, with staggering of start times and quenching of all reactions at the same time. To initiate reactions, catalyst and co-reactants were mixed with pre-incubated RNA, and reactions were performed in a dark incubator. Reactions were quenched by placement on ice and immediately desalted using C_{18} zip-tips, and eluted in 50/50 acetonitrile/water, as described previously.[2]

MALDI-TOF MS Analysis, Peak Assignment, and Quantitation. All MALDI-TOF MS analysis of RNA cleavage was performed using a recently developed method.[2] Briefly, external calibration of the instrument was performed prior to each analysis using a mixture of separate RNA species of varying molecular weights (Fl-5mer, Fl-IRESSLIV, and Fl-RRE, with molecular weights of 2057.5, 8851.5, and 12172.5 Da, respectively), effectively bracketing the range of m/z studied. All MALDI-TOF MS analysis was performed on a Bruker MicroFlex LRF instrument, equipped with a gridless reflectron, using negative ion and reflectron modes. The pulsed ion extraction time was 1200 ns. At least 1000 shots were summed per spectrum. Internal calibrations of smoothed spectra were performed using a set of regularly-occurring MALDI-induced background fragmentation and/or doubly-charged full-length RNA peaks (Supporting Information), and a peak list was generated for each spectrum that contained m/z values and peak areas. Automated peak mass-matching was performed using MassDaddy software, created by Jeff C. Joyner,[2] by comparison of each peak list with the theoretical masses for all expected cleavage products, with a mass-matching tolerance of 200 ppm (Figure SM31, Supporting Information). Only peaks with m/z > 1000 amu were considered in this study. The MS peak areas of all mass-

matched peaks were summed, and the peak area fraction for each peak was determined; only peaks with a peak area fraction above a threshold of 0.0005 were considered (Figure SM32). For time-dependent reactions, the change in peak area fraction (semi-quantitative mole fraction) for each species over time was fit to a first order model, and semi-quantitative apparent initial rates (nM/min) were determined.

Analysis of Radii of Product Distributions. To establish a radius of reactivity (R_{rxn}) for each complex, the center of reactivity (x_c, y_c, z_c) was first established for each complex by use of equation (1), separately for each coordinate (x, y, and z). A weighted average of each Cartesian coordinate (x_c, y_c, and z_c, separately) was determined using the Cartesian coordinates (x_i, y_i, and z_i) of each 4'-C in the entire NMR structure of the Rev/RRE complex, using the apparent initial rate of formation (f_i) of each resulting 3'-phosphoglycolate (3'-PG) from each position within the RNA sequence as a relative weighting for that site.

$$x_c = \frac{\sum_i^N (x_i * f_i)}{\sum_i^N (f_i)} \tag{1}$$

Next, the distance (r_i) of each 4'-C from the calculated center of reactivity (x_c, y_c, z_c) was determined by use of equation (2).

$$r_i = [(x_i - x_c)^2 + (y_i - y_c)^2 + (z_i - z_c)^2]^{\frac{1}{2}} \tag{2}$$

Finally, the apparent initial rate of formation (f_i) of each 3'-PG was plotted as a function of the distance (r_i) of each corresponding 4'-C from the center of reactivity. The resulting data were fit to the Gaussian equation (3), with the distribution centered at $r = 0$, where f is the apparent initial rate of formation of 3'-PG, r is the distance between the corresponding 4'-C and calculated center of reactivity, A is the peak area, and R_{rxn} is the calculated Gaussian radius of reactivity.

$$f = \frac{A}{2 \cdot R_{rxn} \cdot (\frac{\pi}{2})^{\frac{1}{2}}} * e^{-2(\frac{r}{2 \cdot R_{rxn}})^2} \tag{3}$$

Thiobarbituric Acid Assay. Incubations of each M-chelate-Rev catalyst (10 μM) and co-reactants (1 mM H_2O_2 + 1 mM ascorbic acid), with and without unlabelled RRE RNA (10 μM), were performed as described in other sections, for 1 h at 37 ºC. Following incubation, the reaction mixture (20 μL) was immediately mixed with 40 μL 25 % HCl and 40 μL of a solution containing 0.1 % thiobarbituric acid (w/v) in 50 mM NaOH, and the resulting mixture (100 μL) was immediately boiled for 30 min. The mixture was then allowed to cool to RT, stirred, and added to a fluorescence cuvette. The fluorescence emission at 550 nm was monitored, with excitation at 532 nm, on a Varian Cary Eclipse fluorescence spectrophotometer. For each M-chelate-Rev catalyst, two reactions were performed in parallel: one with RNA and one without RNA. The fluorescence intensity without added RNA was subtracted from the fluorescence intensity with added RNA, and this difference was attributed to the 2-hydroxypropene-bis(thiobarbituric acid) adduct formed during the boiling process. All thiobarbituric acid experiments were performed in either duplicate or triplicate.

Fluorescence-Monitored Titrations and Stopped-Flow Measurements Using AP-RRE. The dissociation constants (K_D) for binding of metal ions or complexes to AP-RRE were determined by fluorimetry on a Varian Cary Eclipse fluorescence spectrophotometer with excitation at 310 nm (SW = 10 nm) and emission at 371 nm (SW = 10 nm). A 660 µL volume of 100 nM AP-RRE was first heated to 90 °C for 5 min and then allowed to cool to, but not below, the titration temperature (37 °C). A 650 µL volume of this sample was added to the pre-thermostatted cuvette. After 10 min of temperature equilibration a solution of metal ion/complex was titrated into the AP-RRE solution. After each addition, 100 µL of the solution was mixed by gentle pipetting to ensure complete mixing. The fluorescence change of AP-RRE upon Cu-binding was monitored. Titration response curves were dilution-corrected, normalized to initial intensity values, and fit to eqn (4), where F_{obsd} is the observed fluorescence intensity, F_{bound} is the fluorescence of metal-bound RNA, F_{free} is the fluorescence of unbound RNA, [M] is the concentration of added metal ion or complex, K_D is the fitted dissociation constant, and n is the fitted cooperativity (Figure SM26, Supporting Information).

$$F_{obsd} = F_{bound} + (F_{free}-F_{bound})/[1 + ([M]/K_D)^n] \quad (4)$$

Stopped-flow measurements of the kinetics of Cu^{2+}(aq) binding to AP-RRE were made using an Applied Photophysics SpectraKinetic Monochromator, with excitation at 310 nm and an emission filer with band pass > 360 nm. Two syringes were used, one containing 100 nM AP-RRE and the other containing variable concentrations of Cu^{2+}(aq). Data were collected only after two purge injections, and each kinetic trace of fluorescence vs time (log time) was the average of 3 trials. Kinetic traces were fit to a pentaphasic first order kinetic model (Figure SM26, Supporting Information).

INITIAL RATES OF CLEAVAGE OF RRE RNA (MALDI-TOF MS)

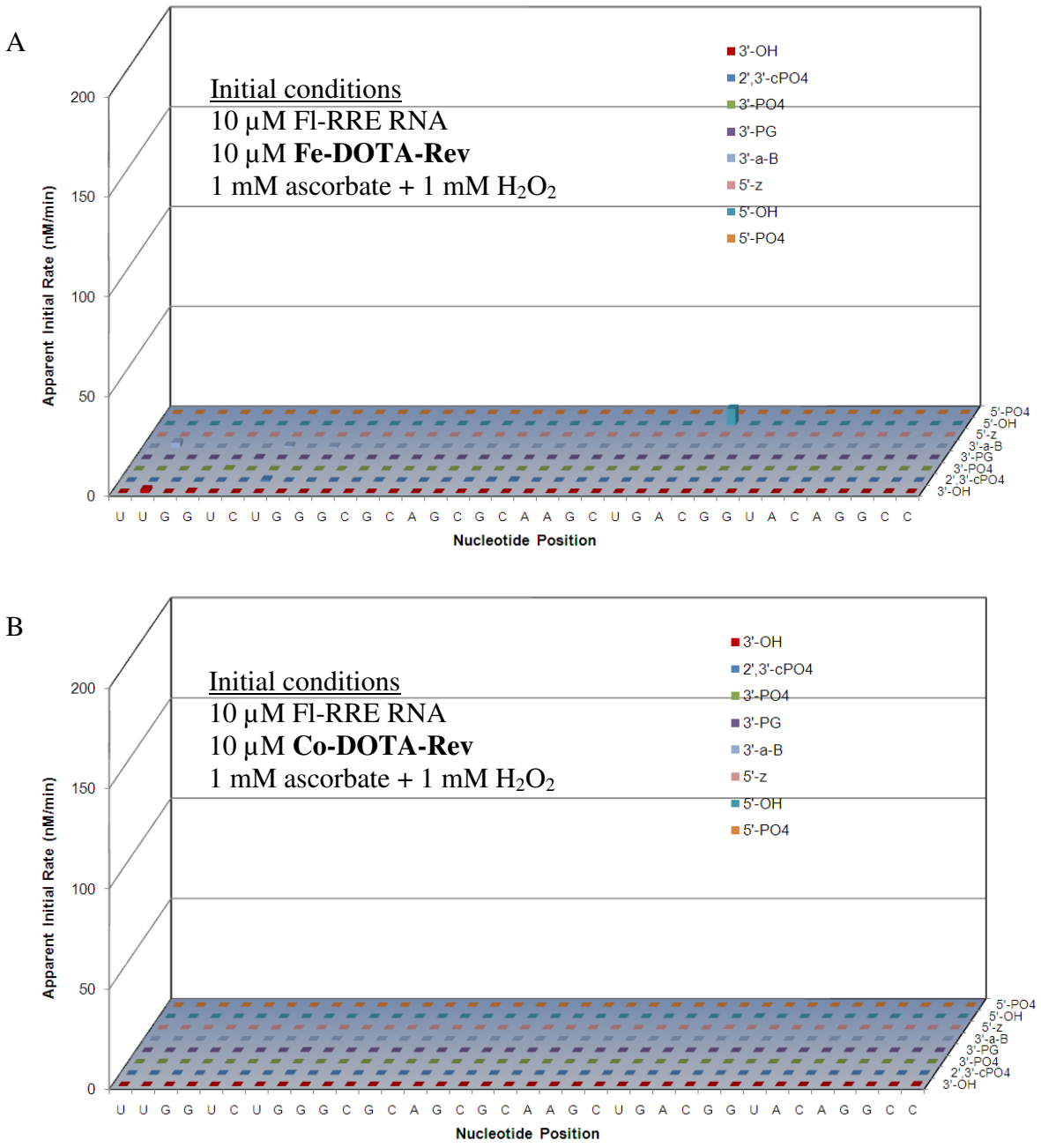

Figure SM1. Apparent initial rates of formation of cleavage products, for cleavage at all nucleotide positions within the RRE RNA, and for fragments with each type of nascent terminal overhang, following time-dependent cleavage of Fl-RRE RNA by (A) Fe-DOTA-Rev and (B) Co-DOTA-Rev, each in the presence of co-reactants. Time-dependent experiments were monitored by MALDI-TOF MS (~ 8 mass spectra per catalyst). The apparent initial rate of disappearance of the full-length Fl-RRE RNA is shown at the front/right position (3'-OH).

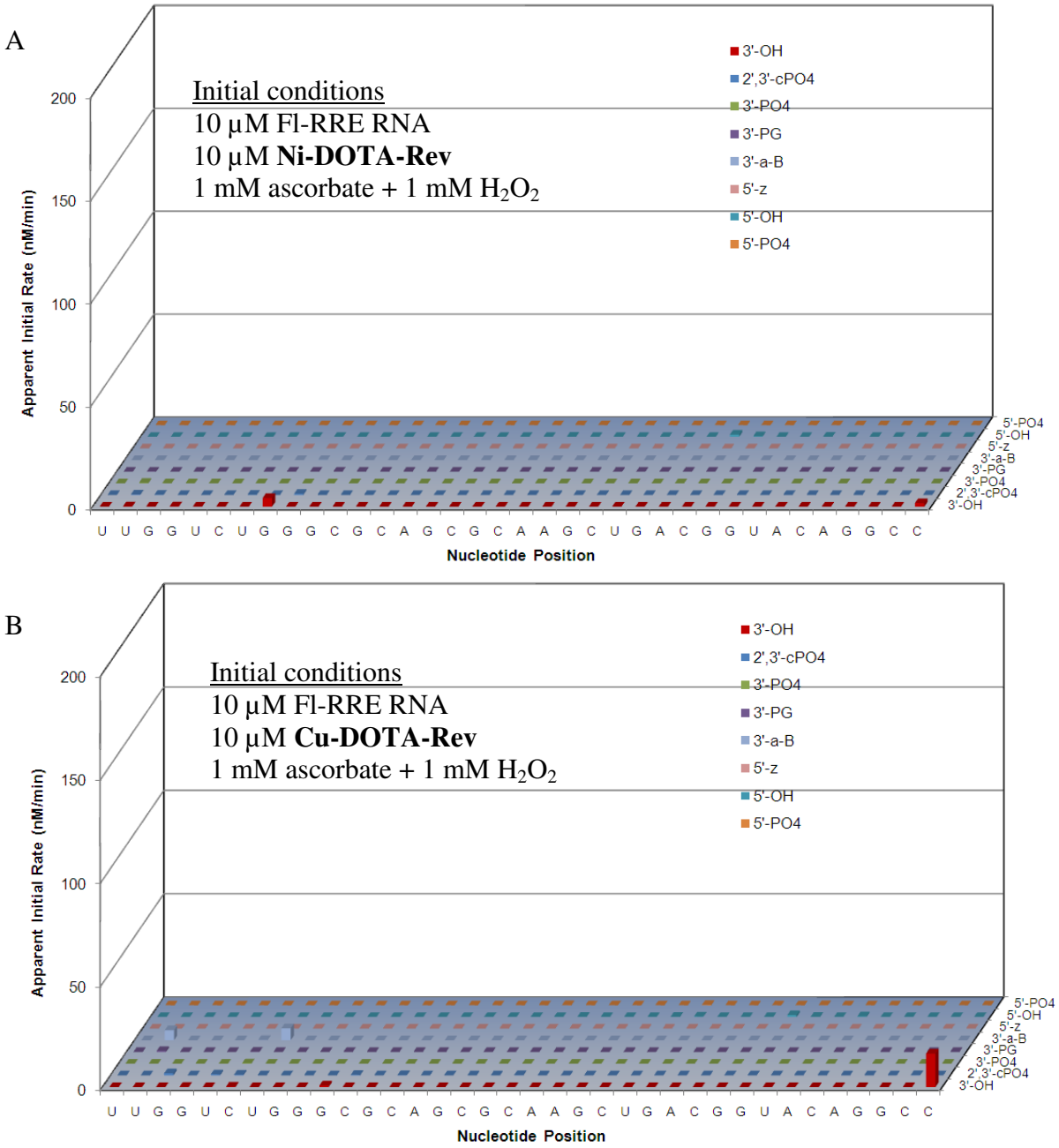

Figure SM2. Apparent initial rates of formation of cleavage products, for cleavage at all nucleotide positions within the RRE RNA, and for fragments with each type of nascent terminal overhang, following time-dependent cleavage of Fl-RRE RNA by (A) Ni-DOTA-Rev and (B) Cu-DOTA-Rev, each in the presence of co-reactants. Time-dependent experiments were monitored by MALDI-TOF MS (~ 8 mass spectra per catalyst). The apparent initial rate of disappearance of the full-length Fl-RRE RNA is shown at the front/right position (3'-OH).

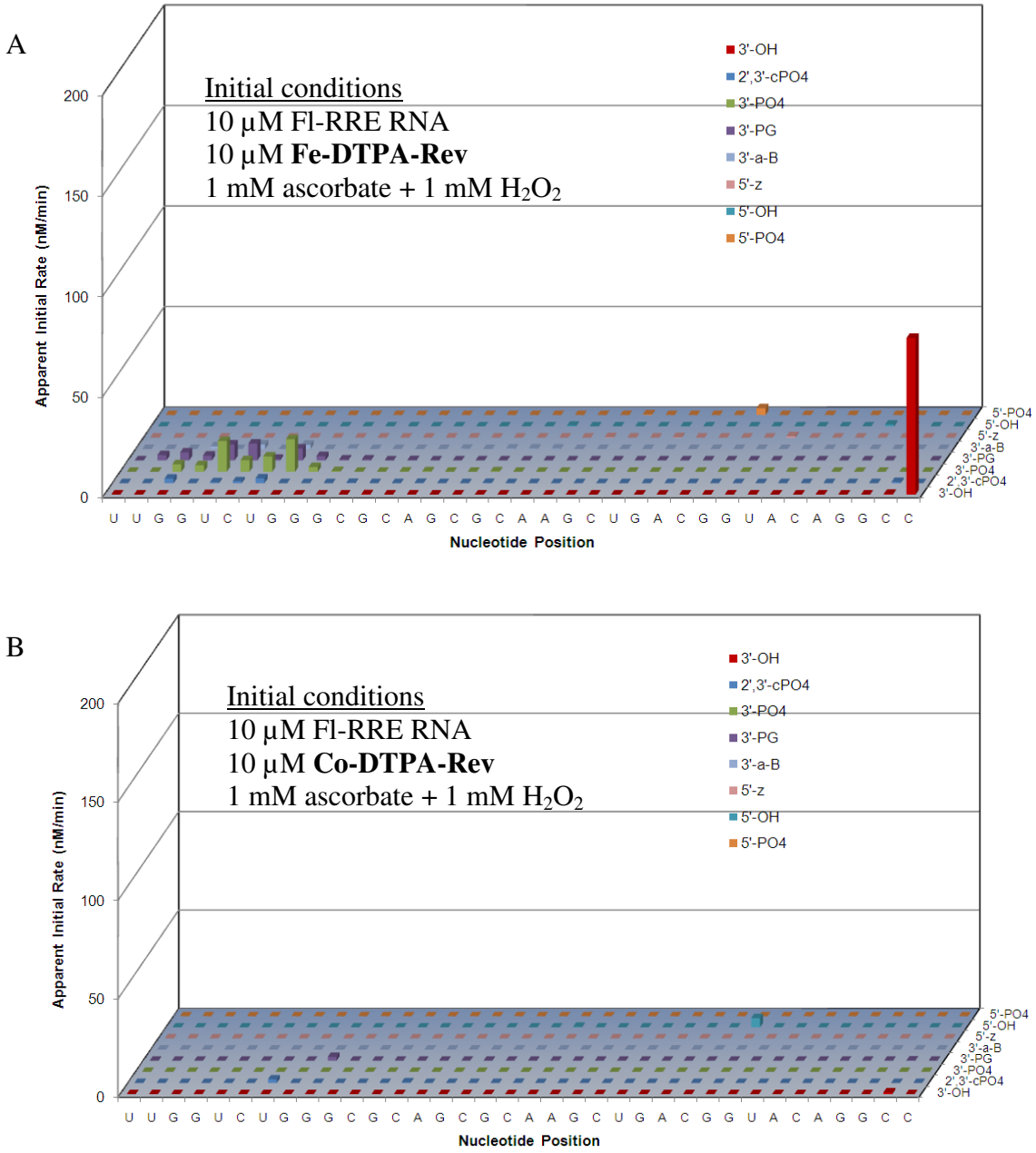

Figure SM3. Apparent initial rates of formation of cleavage products, for cleavage at all nucleotide positions within the RRE RNA, and for fragments with each type of nascent terminal overhang, following time-dependent cleavage of Fl-RRE RNA by (A) Fe-DTPA-Rev and (B) Co-DTPA-Rev, each in the presence of co-reactants. Time-dependent experiments were monitored by MALDI-TOF MS (~ 8 mass spectra per catalyst). The apparent initial rate of disappearance of the full-length Fl-RRE RNA is shown at the front/right position (3'-OH).

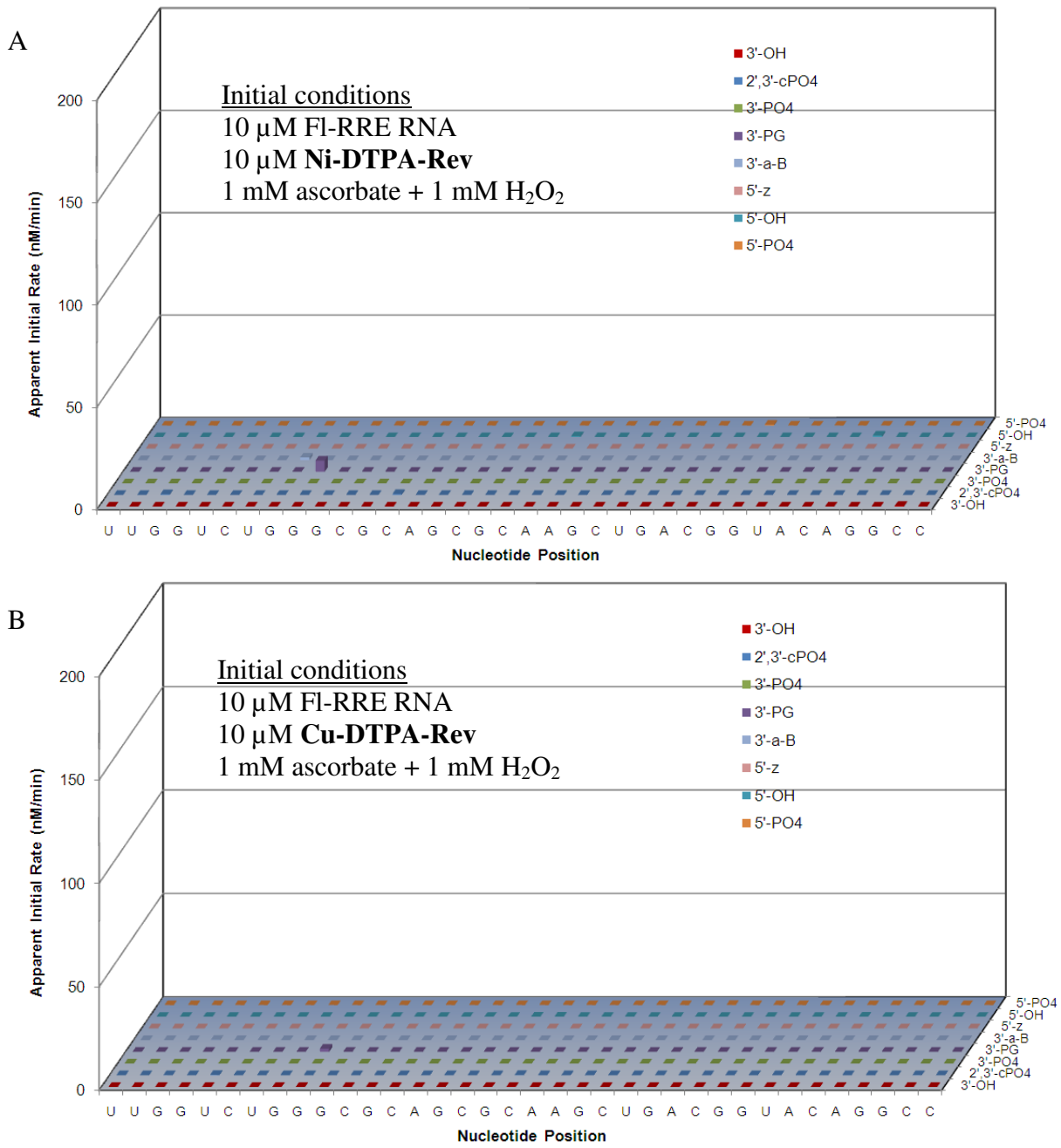

Figure SM4. Apparent initial rates of formation of cleavage products, for cleavage at all nucleotide positions within the RRE RNA, and for fragments with each type of nascent terminal overhang, following time-dependent cleavage of Fl-RRE RNA by (A) Ni-DTPA-Rev and (B) Cu-DTPA-Rev, each in the presence of co-reactants. Time-dependent experiments were monitored by MALDI-TOF MS (~ 8 mass spectra per catalyst). The apparent initial rate of disappearance of the full-length Fl-RRE RNA is shown at the front/right position (3'-OH).

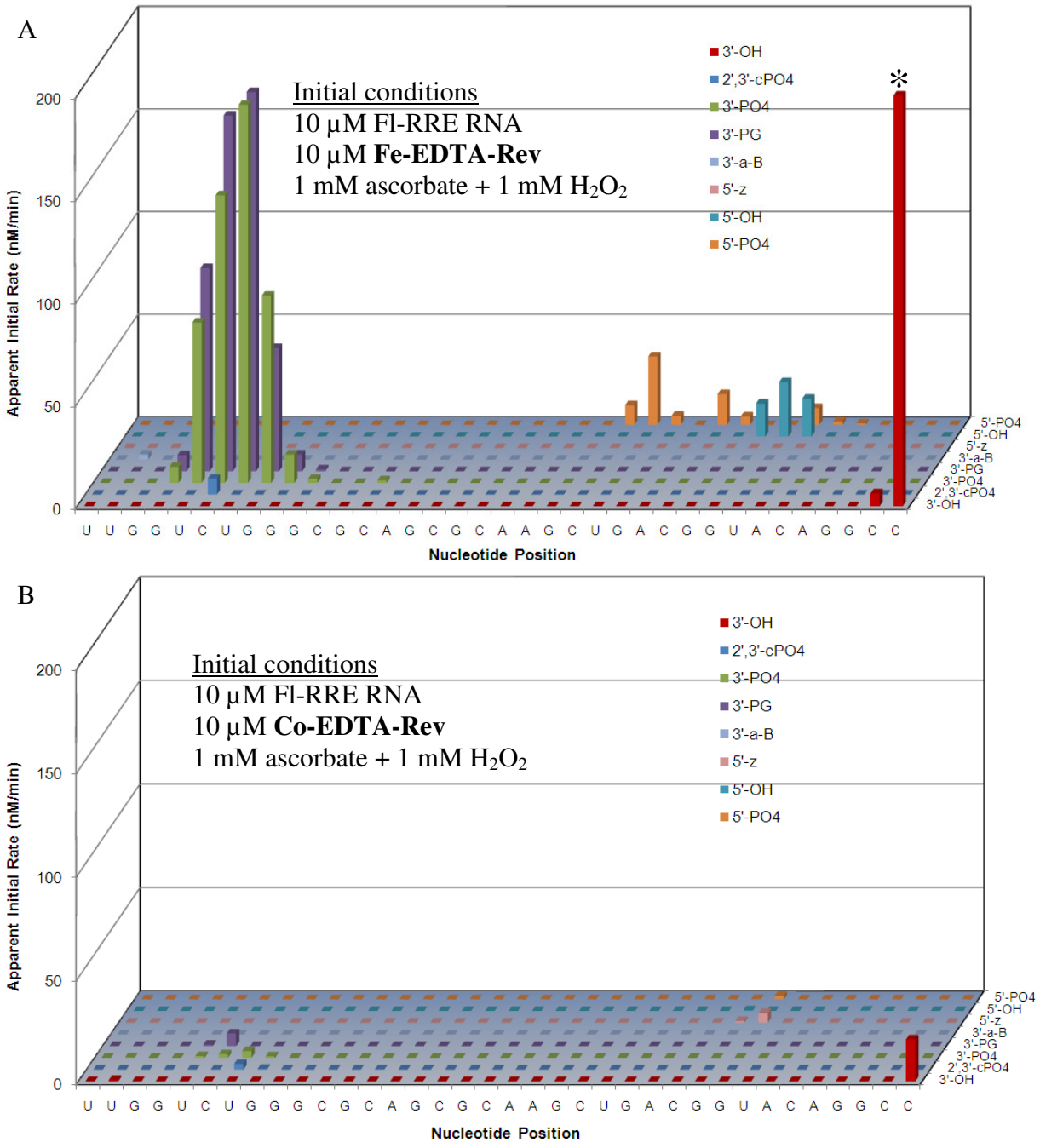

Figure SM5. Apparent initial rates of formation of cleavage products, for cleavage at all nucleotide positions within the RRE RNA, and for fragments with each type of nascent terminal overhang, following time-dependent cleavage of Fl-RRE RNA by (A) Fe-EDTA-Rev and (B) Co-EDTA-Rev, each in the presence of co-reactants. Time-dependent experiments were monitored by MALDI-TOF MS (~ 8 mass spectra per catalyst). The apparent initial rate of disappearance of the full-length Fl-RRE RNA is shown at the front/right position (3'-OH). * The apparent initial rate of disappearance of the full-length Fl-RRE RNA is truncated in the figure for Fe-EDTA-Rev.

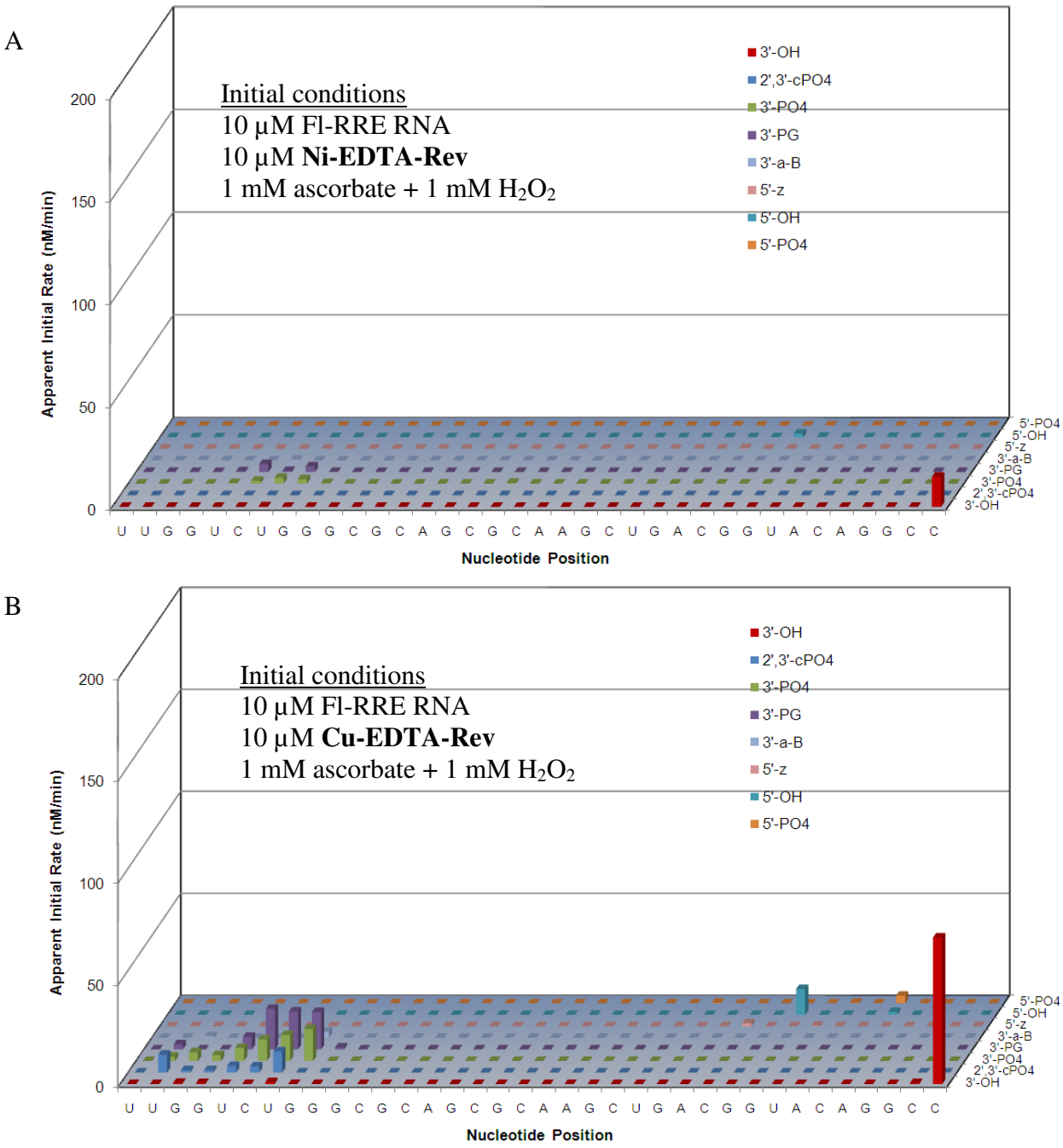

Figure SM6. Apparent initial rates of formation of cleavage products, for cleavage at all nucleotide positions within the RRE RNA, and for fragments with each type of nascent terminal overhang, following time-dependent cleavage of Fl-RRE RNA by (A) Ni-EDTA-Rev and (B) Cu-EDTA-Rev, each in the presence of co-reactants. Time-dependent experiments were monitored by MALDI-TOF MS (~ 8 mass spectra per catalyst). The apparent initial rate of disappearance of the full-length Fl-RRE RNA is shown at the front/right position (3'-OH).

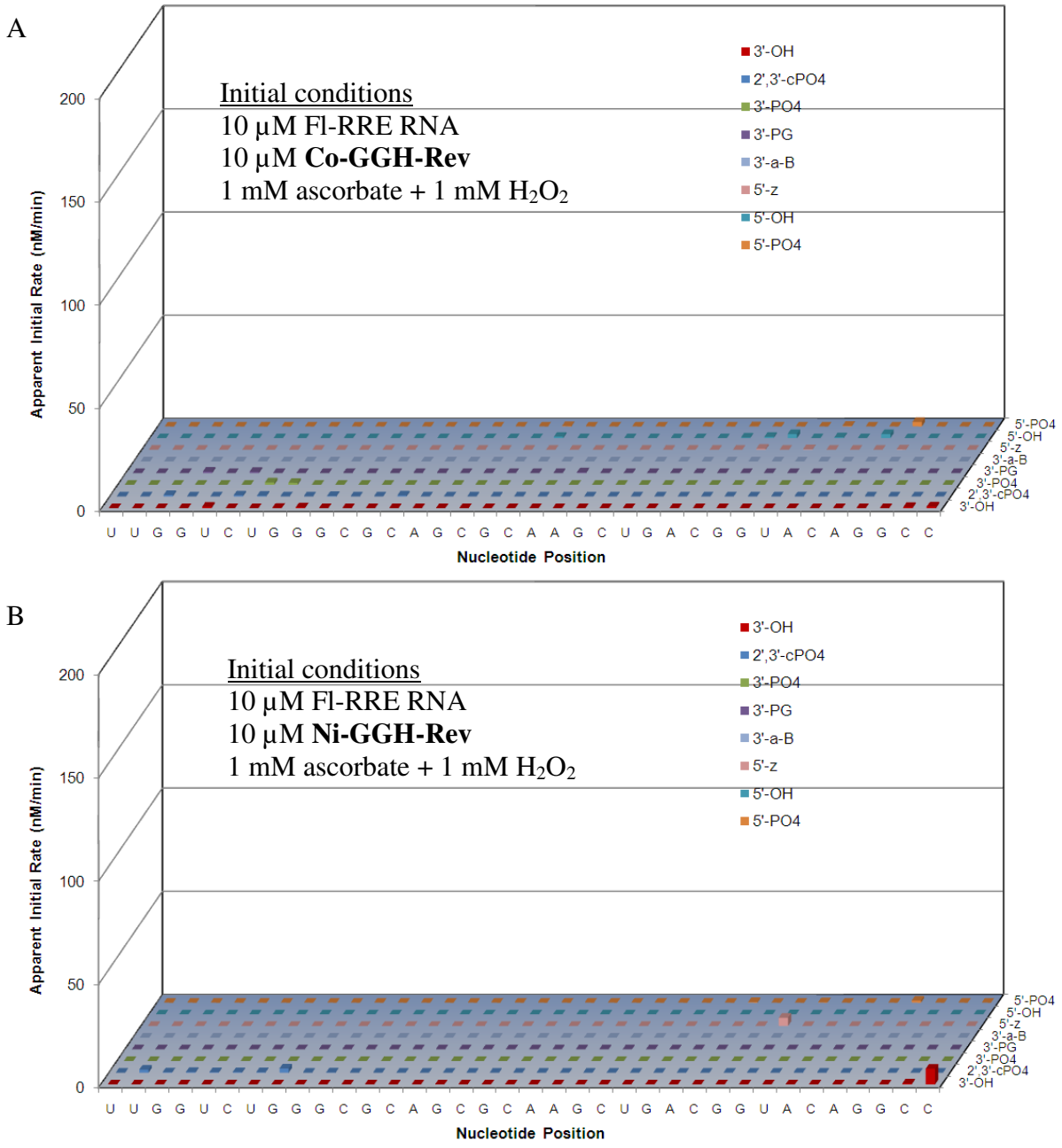

Figure SM7. Apparent initial rates of formation of cleavage products, for cleavage at all nucleotide positions within the RRE RNA, and for fragments with each type of nascent terminal overhang, following time-dependent cleavage of Fl-RRE RNA by (A) Co-GGH-Rev and (B) Ni-GGH-Rev, each in the presence of co-reactants. Time-dependent experiments were monitored by MALDI-TOF MS (~ 8 mass spectra per catalyst). The apparent initial rate of disappearance of the full-length Fl-RRE RNA is shown at the front/right position (3'-OH).

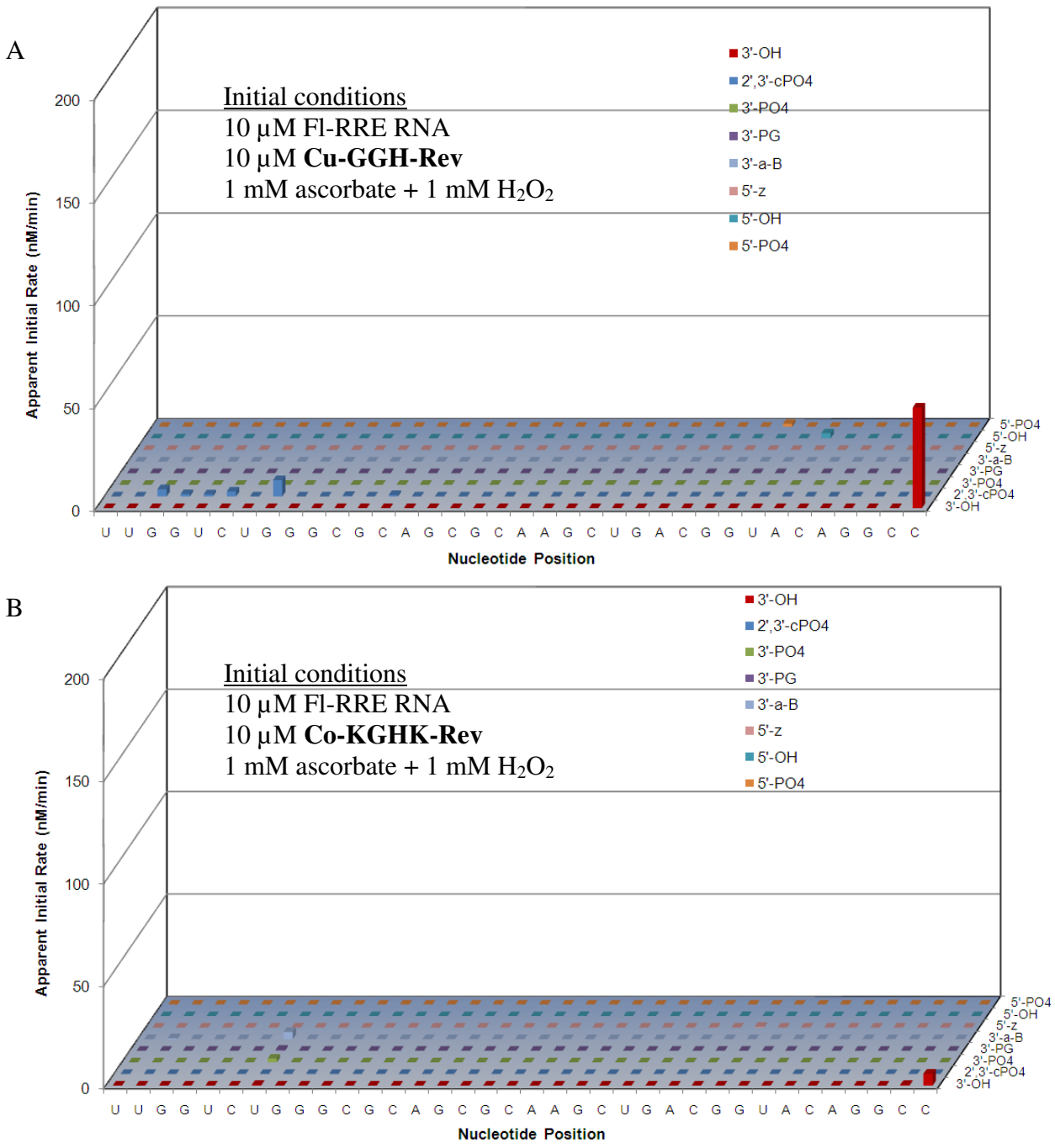

Figure SM8. Apparent initial rates of formation of cleavage products, for cleavage at all nucleotide positions within the RRE RNA, and for fragments with each type of nascent terminal overhang, following time-dependent cleavage of Fl-RRE RNA by (A) Cu-GGH-Rev and (B) Co-KGHK-Rev, each in the presence of co-reactants. Time-dependent experiments were monitored by MALDI-TOF MS (~ 8 mass spectra per catalyst). The apparent initial rate of disappearance of the full-length Fl-RRE RNA is shown at the front/right position (3'-OH).

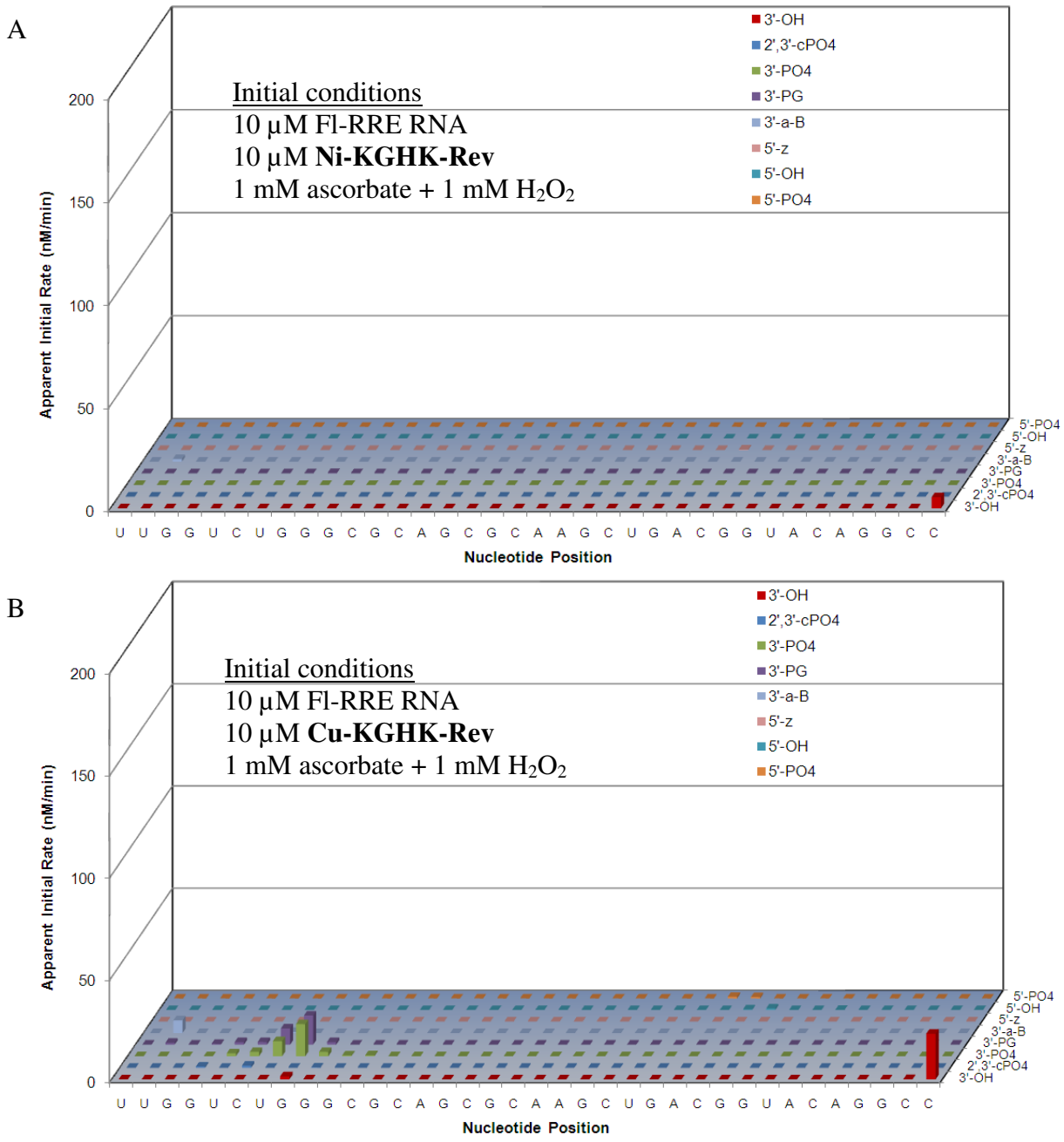

Figure SM9. Apparent initial rates of formation of cleavage products, for cleavage at all nucleotide positions within the RRE RNA, and for fragments with each type of nascent terminal overhang, following time-dependent cleavage of Fl-RRE RNA by (A) Ni-KGHK-Rev and (B) Cu-KGHK-Rev, each in the presence of co-reactants. Time-dependent experiments were monitored by MALDI-TOF MS (~ 8 mass spectra per catalyst). The apparent initial rate of disappearance of the full-length Fl-RRE RNA is shown at the front/right position (3'-OH).

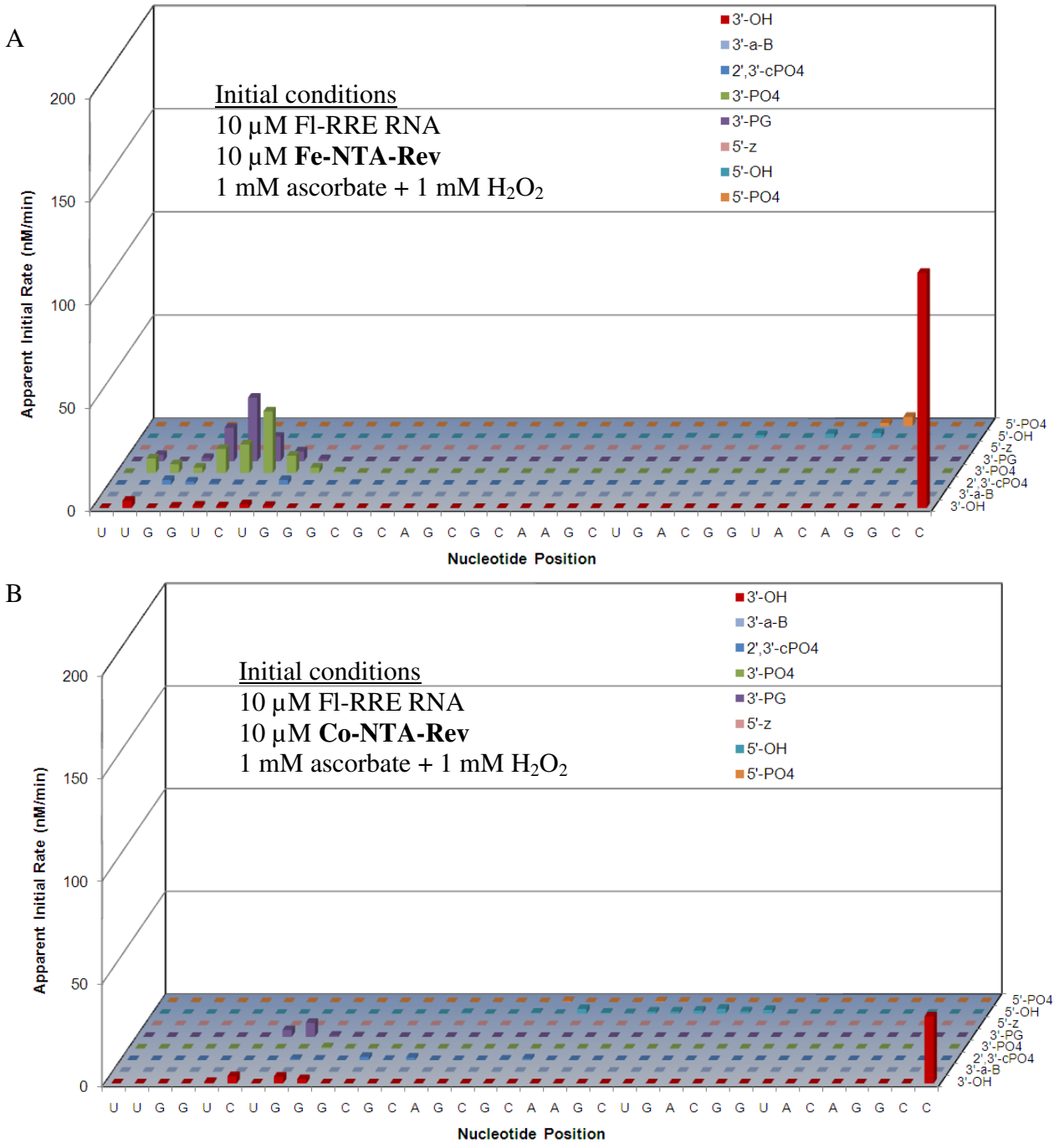

Figure SM10. Apparent initial rates of formation of cleavage products, for cleavage at all nucleotide positions within the RRE RNA, and for fragments with each type of nascent terminal overhang, following time-dependent cleavage of Fl-RRE RNA by (A) Fe-NTA-Rev and (B) Co-NTA-Rev, each in the presence of co-reactants. Time-dependent experiments were monitored by MALDI-TOF MS (~ 8 mass spectra per catalyst). The apparent initial rate of disappearance of the full-length Fl-RRE RNA is shown at the front/right position (3'-OH).

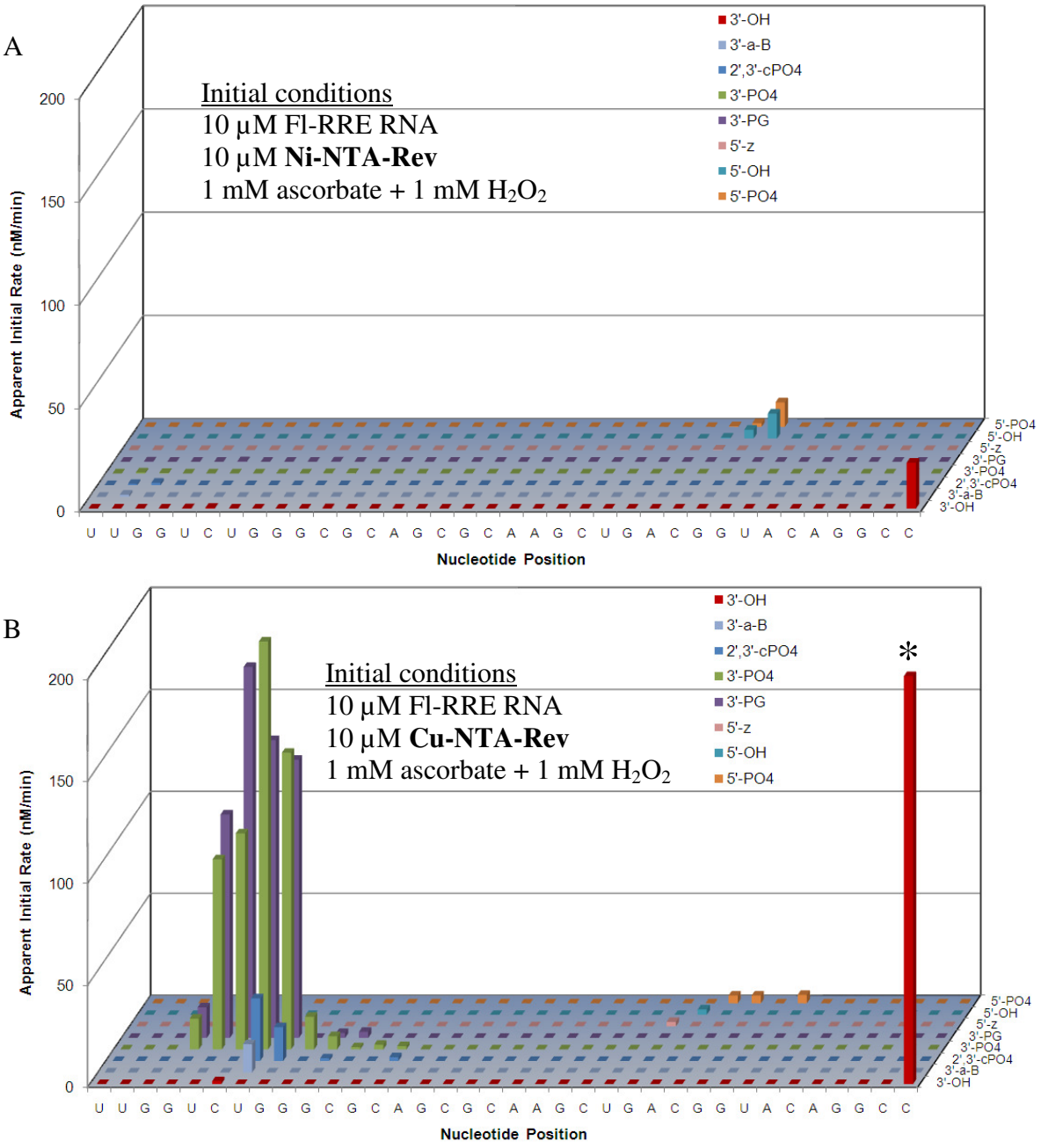

Figure SM11. Apparent initial rates of formation of cleavage products, for cleavage at all nucleotide positions within the RRE RNA, and for fragments with each type of nascent terminal overhang, following time-dependent cleavage of Fl-RRE RNA by (A) Ni-NTA-Rev and (B) Cu-NTA-Rev, each in the presence of co-reactants. Time-dependent experiments were monitored by MALDI-TOF MS (~ 8 mass spectra per catalyst). The apparent initial rate of disappearance of the full-length Fl-RRE RNA is shown at the front/right position (3'-OH). * The apparent initial rate of disappearance of the full-length Fl-RRE RNA is truncated in the figure for Cu-NTA-Rev.

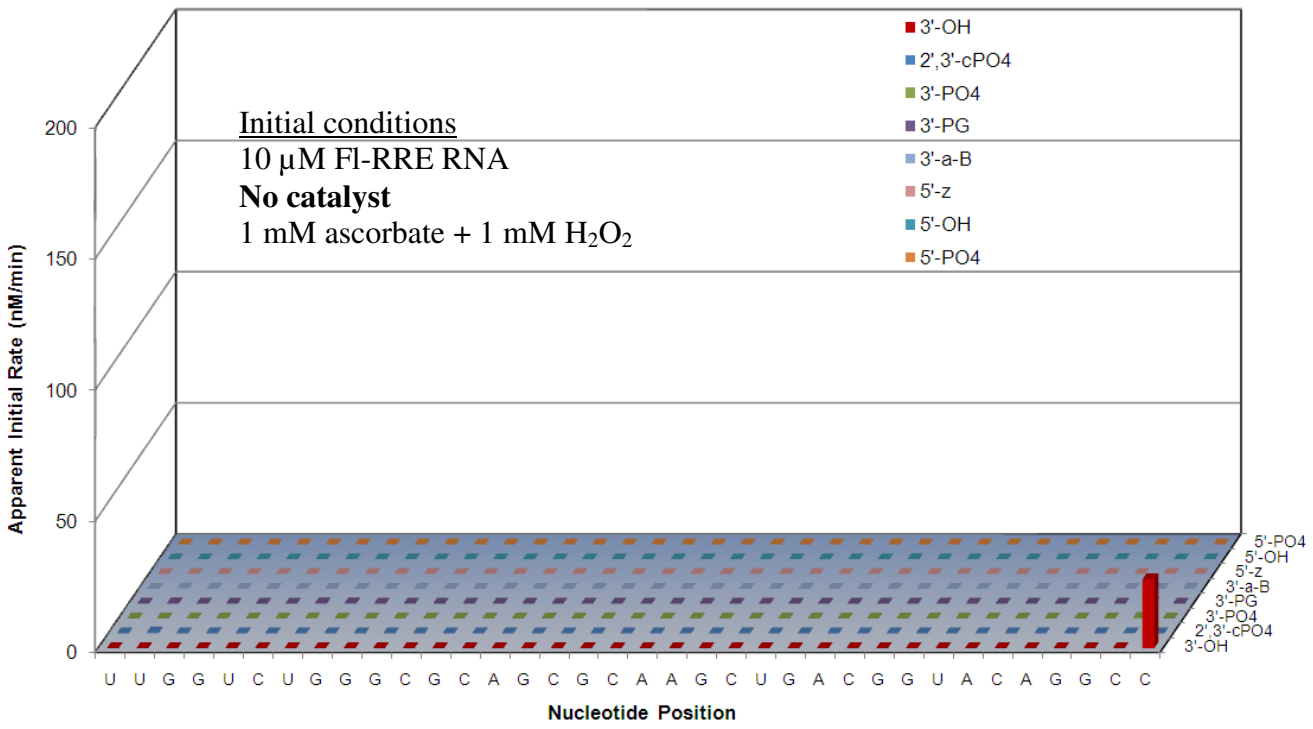

Figure SM12. Apparent initial rates of formation of cleavage products, for cleavage at all nucleotide positions within the RRE RNA, and for fragments with each type of nascent terminal overhang, following time-dependent cleavage of Fl-RRE RNA in the absence of catalyst, but in the presence of co-reactants. Time-dependent experiments were monitored by MALDI-TOF MS (~ 8 mass spectra per catalyst). The apparent initial rate of disappearance of the full-length Fl-RRE RNA is shown at the front/right position (3'-OH).

Complex	3'-OH	2',3'-cPO$_4$	3'-PO$_4$	3'-PG	3'-a-B	5'-OH	5'-PO$_4$	5'-z	RRE - 1B	RRE + (O)n	Total
Fe-DOTA-Rev	2.1	1.8	0.6	0.3	4.1	8.4	0.1	0.0	0.6	1.1	19.2
Fe-DTPA-Rev	0.4	7.0	55.1	35.3	7.0	1.2	3.7	1.2	2.1	6.4	119.2
Fe-EDTA-Rev	0.0	7.7	518.3	533.9	2.6	60.9	77.0	0.0	0.0	1.0	1201.4
Fe-NTA-Rev	8.9	7.2	81.2	69.4	0.0	6.5	6.3	0.1	0.0	0.0	179.5
Co-DOTA-Rev	0.0	0.4	0.1	0.2	0.3	0.2	0.1	0.3	0.0	3.1	4.7
Co-DTPA-Rev	0.1	2.3	0.1	2.0	0.0	5.0	0.0	0.0	0.0	2.0	11.4
Co-EDTA-Rev	0.6	3.1	6.8	6.9	0.0	0.5	1.7	5.5	3.0	0.0	28.1
Co-GGH-Rev	1.1	2.1	2.0	1.6	0.0	5.8	2.7	1.0	1.0	3.8	21.2
Co-KGHK-Rev	0.3	0.0	1.9	0.5	4.1	0.1	0.1	0.4	2.3	14.8	24.5
Co-NTA-Rev	9.4	4.8	0.5	11.1	0.0	13.1	1.1	0.0	0.0	39.7	79.9
Ni-DOTA-Rev	4.4	0.9	0.3	0.1	0.1	1.4	0.0	0.0	0.1	0.0	7.2
Ni-DTPA-Rev	0.0	0.7	0.0	5.4	1.4	1.1	0.4	0.0	0.0	0.0	9.1
Ni-EDTA-Rev	0.2	0.0	7.0	7.4	0.6	2.1	0.3	0.3	1.7	17.1	36.6
Ni-GGH-Rev	0.0	4.8	0.0	0.0	0.0	0.2	1.4	4.0	0.4	12.8	23.7
Ni-KGHK-Rev	0.0	0.1	0.2	0.1	1.3	0.0	0.1	0.3	4.1	10.2	16.3
Ni-NTA-Rev	0.5	2.1	1.0	0.5	1.1	17.6	14.1	0.4	0.2	11.4	49.0
Cu-DOTA-Rev	1.1	2.4	0.2	0.6	10.8	1.6	0.3	0.0	1.7	38.5	57.2
Cu-DTPA-Rev	0.0	0.3	0.0	1.5	0.2	0.1	0.0	0.0	2.0	8.3	12.4
Cu-EDTA-Rev	1.9	27.5	54.5	66.3	3.8	14.0	4.4	1.9	0.0	14.7	189.0
Cu-GGH-Rev	0.0	16.9	0.0	0.0	0.0	2.5	1.5	0.0	0.0	33.1	54.0
Cu-KGHK-Rev	1.4	1.7	29.5	27.3	6.8	1.0	1.5	0.0	0.2	15.9	85.3
Cu-NTA-Rev	1.4	50.3	600.1	593.9	13.8	2.6	11.7	2.2	0.0	2.5	1278.6
None	0.0	0.3	0.4	0.7	0.1	0.0	0.0	0.0	10.8	21.2	33.6

Table SM1. Tabular form of the data shown in figure 7 of the manuscript. Breakdown of the apparent initial rates of formation of RNA cleavage fragments containing each type of nascent terminal overhang, resulting from cleavage of Fl-RRE RNA by each M-chelate-Rev complex, in the presence of co-reactants. Time-dependent experiments were monitored by MALDI-TOF MS (typically 8 mass spectra per catalyst). Also included were the apparent initial rates of formation of full-length RNA with either missing bases or one or more additions of oxygen. The quantified nascent terminal overhang types were 3'-OH, 2',3'-cPO$_4$, 3'-PO$_4$, 3'-PG, 3'-a-B, 5'-z, 5'OH, and 5'-PO$_4$. In order to obtain the apparent initial rate of formation for a given overhang type, the apparent rates of formation for that product type at all positions within the RNA sequence were summed.

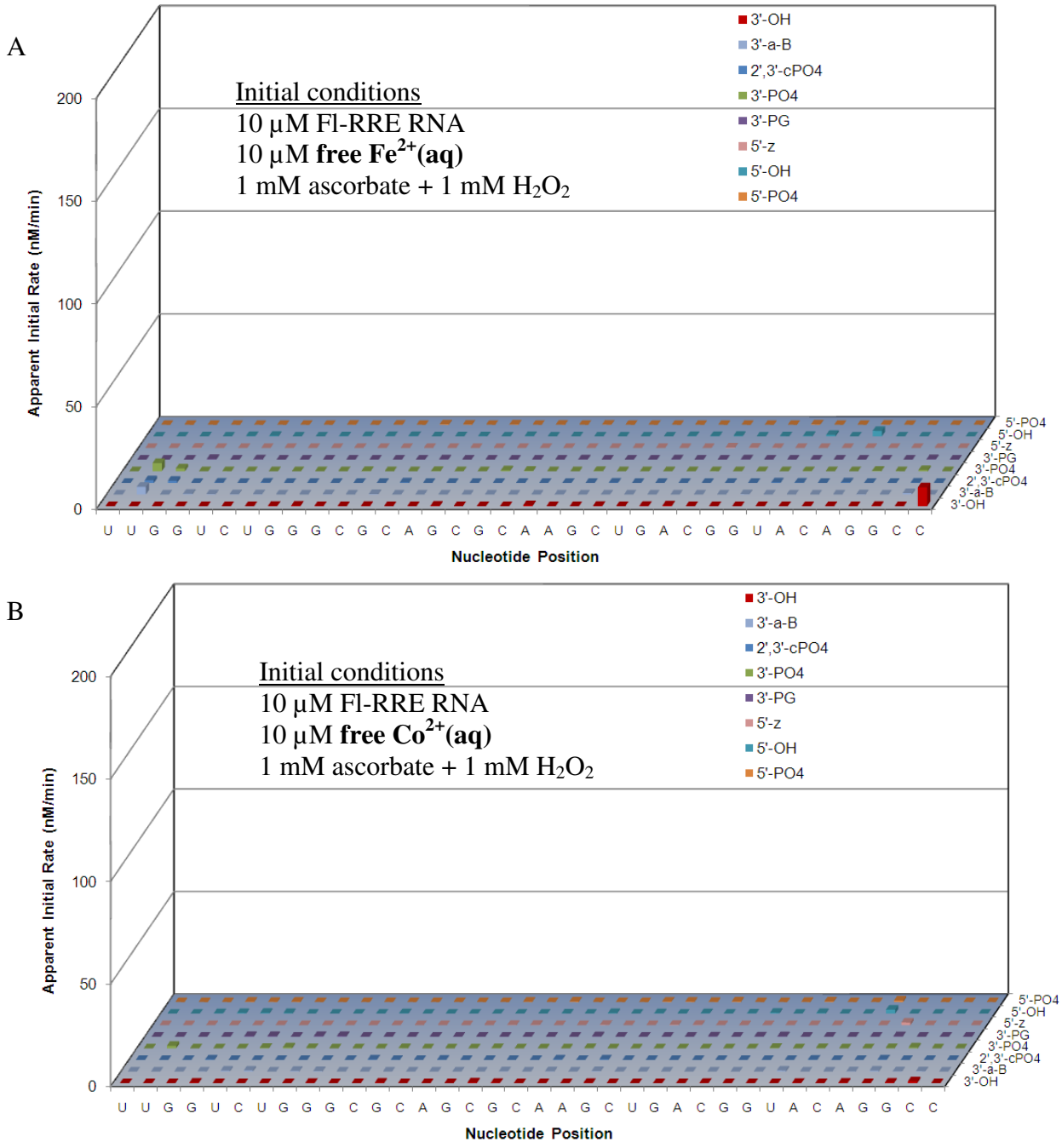

Figure SM13. Apparent initial rates of formation of cleavage products, for cleavage at all nucleotide positions within the RRE RNA, and for fragments with each type of nascent terminal overhang, following time-dependent cleavage of Fl-RRE RNA by (A) free Fe^{2+}(aq) and (B) free Co^{2+}(aq), each in the presence of co-reactants. Time-dependent experiments were monitored by MALDI-TOF MS (~ 8 mass spectra per catalyst). The apparent initial rate of disappearance of the full-length Fl-RRE RNA is shown at the front/right position (3'-OH).

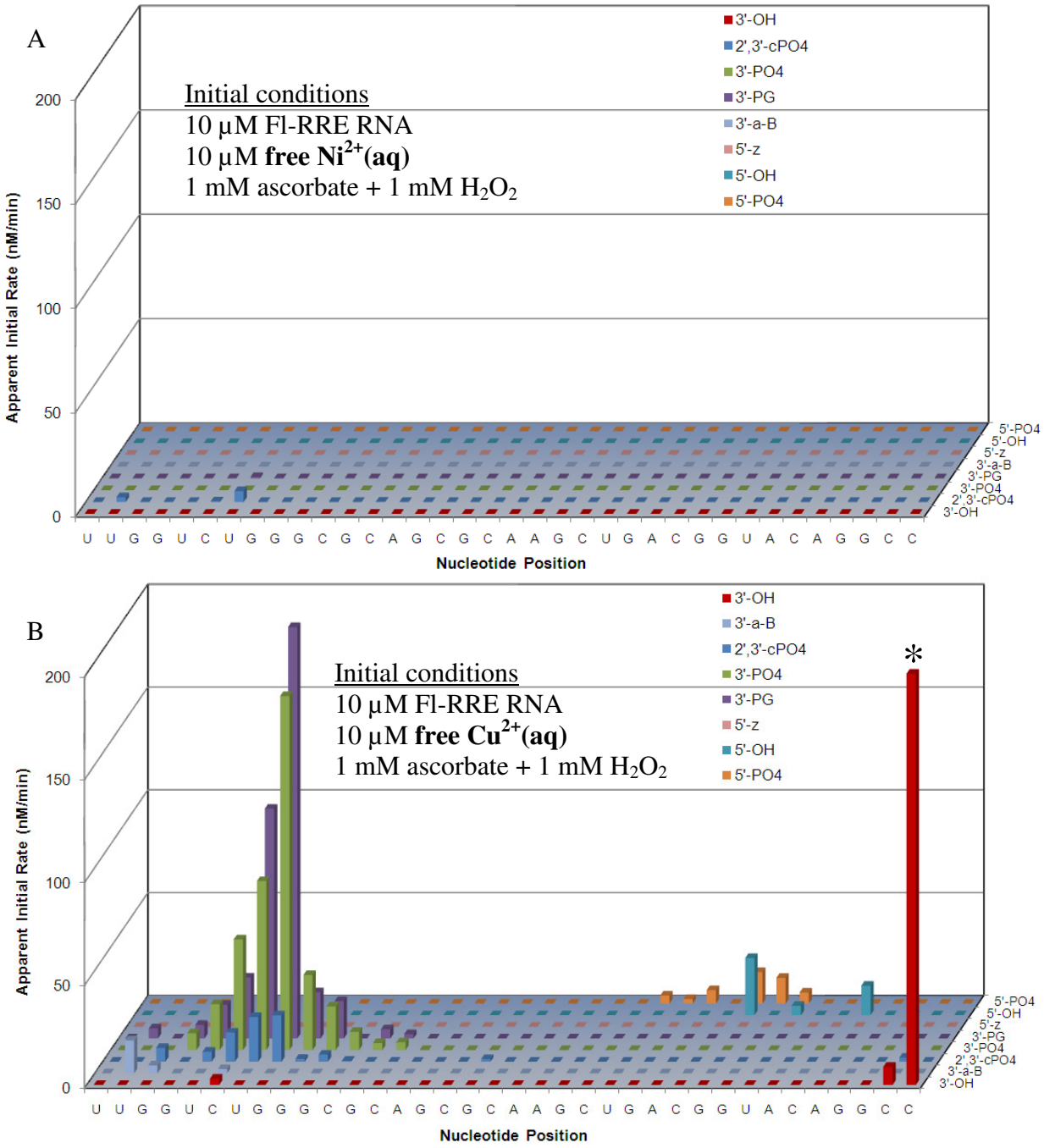

Figure SM14. Apparent initial rates of formation of cleavage products, for cleavage at all nucleotide positions within the RRE RNA, and for fragments with each type of nascent terminal overhang, following time-dependent cleavage of Fl-RRE RNA by (A) free Ni^{2+}(aq) and (B) free Cu^{2+}(aq), each in the presence of co-reactants. Time-dependent experiments were monitored by MALDI-TOF MS (~ 8 mass spectra per catalyst). The apparent initial rate of disappearance of the full-length Fl-RRE RNA is shown at the front/right position (3'-OH). The relatively high activity of free Cu^{2+}(aq) was the result of the combination of a low-affinity Cu-binding site within the RRE RNA (discussed later) and the high concentrations of catalyst and RNA required for MALDI-TOF MS detection (10 µM). The distribution of cleavage sites/rates for free Cu^{2+}(aq) is distinct from the M-chelate-Rev catalysts. * The rate of disappearance of the full-length Fl-RRE RNA is truncated in the figure for free Cu^{2+}(aq).

catalyst	Apparent Initial Rate of RNA Modification (nM/min)			
	MALDI method 1	MALDI method 2	PAGE	AP-RRE [a]
Fe-DOTA-Rev	9	0	8 ± 2	n.d.
Fe-DTPA-Rev	100	80	190 ± 40	n.d.
Fe-EDTA-Rev	1100	500	4000 ± 1000	5200 ± 100
Fe-NTA-Rev	200	100	250 ± 40	3200 ± 100
Co-DOTA-Rev	1	0.2	< 4	n.d.
Co-DTPA-Rev	4	0	n.d.	n.d.
Co-EDTA-Rev	20	20	6 ± 1	0 ± 1
Co-GGH-Rev	7	1	n.d.	n.d.
Co-KGHK-Rev	7	6	< 11	n.d.
Co-NTA-Rev	30	30	6 ± 2	640 ± 20
Ni-DOTA-Rev	6	2	8 ± 2	n.d.
Ni-DTPA-Rev	8	0	n.d.	n.d.
Ni-EDTA-Rev	20	10	32 ± 6	< 2
Ni-GGH-Rev	5	10	n.d.	n.d.
Ni-KGHK-Rev	2	5	< 15	n.d.
Ni-NTA-Rev	5	20	90 ± 20	n.d.
Cu-DOTA-Rev	20	20	4 ± 3	n.d.
Cu-DTPA-Rev	2	0	n.d.	n.d.
Cu-EDTA-Rev	200	70	46 ± 5	~ 0
Cu-GGH-Rev	20	50	n.d.	n.d.
Cu-KGHK-Rev	70	20	80 ± 50	n.d.
Cu-NTA-Rev	1300	500	300 ± 30	1400 ± 100
Free Fe	20	10	< 4	n.d.
Free Co	10	0	13 ± 2	n.d.
Free Ni	8	n.d.	< 3	n.d.
Free Cu	900	700	900 ± 200	n.d.
None	2	30	< 4	4.0 ± 0.5

Table SM2. Comparison of MALDI-TOF MS, PAGE, and fluorimetry (AP-RNA) assays for quantification of the initial rate of modification of RRE RNA. Reactions contained 10 µM RNA (Fl-RRE RNA for MALDI and PAGE; AP-RNA for the fluorimetry assay), 1 mM H_2O_2/ascorbate, and 10 µM catalyst (if present). [a] The AP-RNA construct corresponds to RRE RNA with an internal 2-aminopurine,[3] the fluorescence of which decreases upon a conformational change in the RNA, following reaction; rates for the AP-RNA assay tend to be higher than for the PAGE assay, due to differences in what is being monitored, as described previously (Joyner et al., 2011).[1]

EXTENTS OF OXIDATIVE CLEAVAGE OF RRE RNA AFTER 1 HOUR INCUBATION (MALDI-TOF MS)

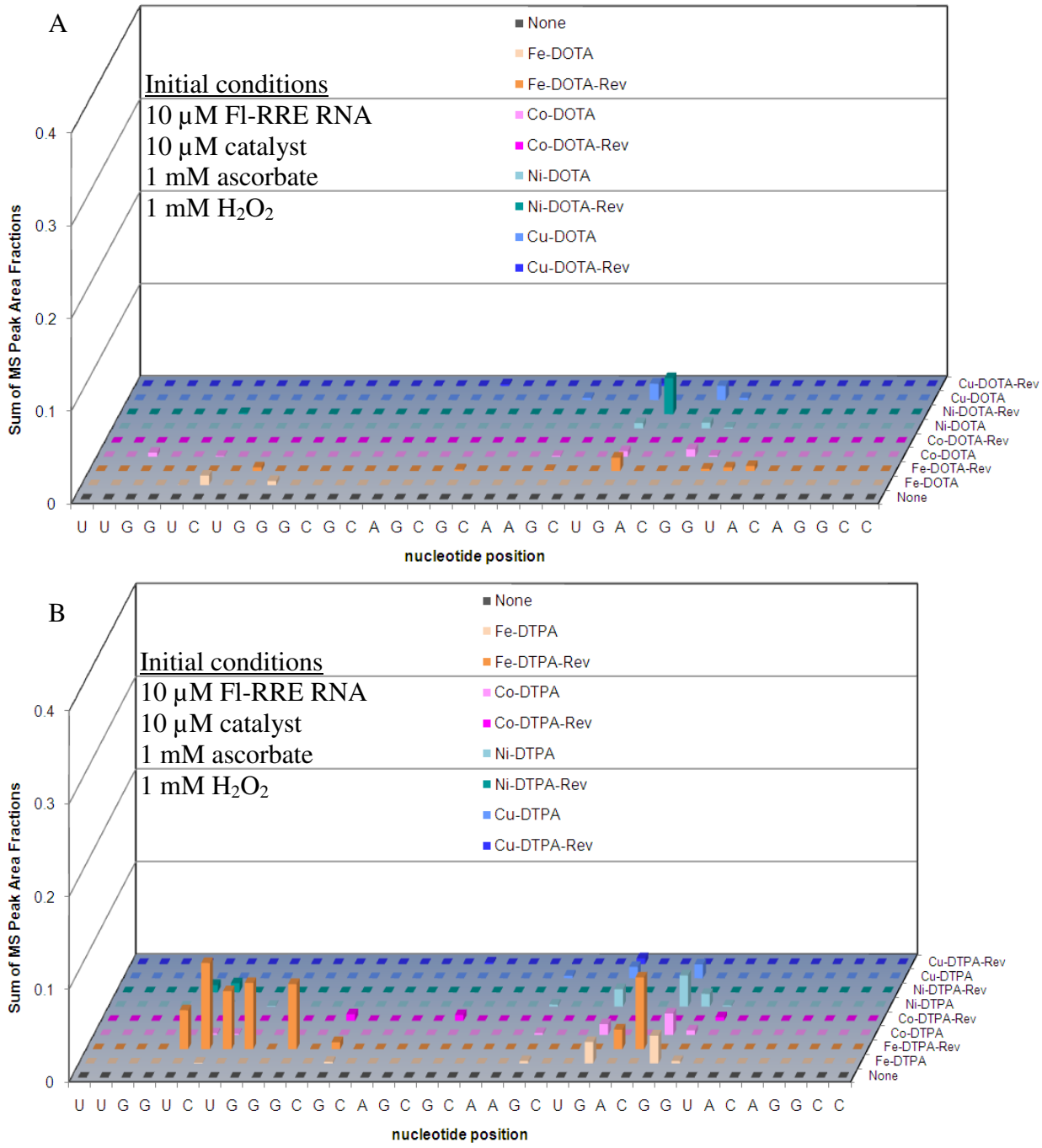

Figure SM15. Targeted cleavage of RRE RNA required attachment of catalysts to the Rev peptide in order to achieve efficient cleavage, as seen by differences in reactivity between the M-chelate-Rev catalysts and M-chelates lacking Rev. (A) M-DOTA-Rev vs M-DOTA and (B) M-DTPA-Rev vs M-DTPA. After 1 h incubation of each catalyst and co-reactants with the Fl-RRE RNA, the apparent abundances of individual RNA cleavage fragments were quantified. The data correspond to the abundances (MS peak area fractions) of oxidation products (cleavage fragments containing nascent terminal 3'-PO_4, 3'-PG, or 5'-PO_4 overhangs), at positions adjacent to each illustrated site of H-abstraction.

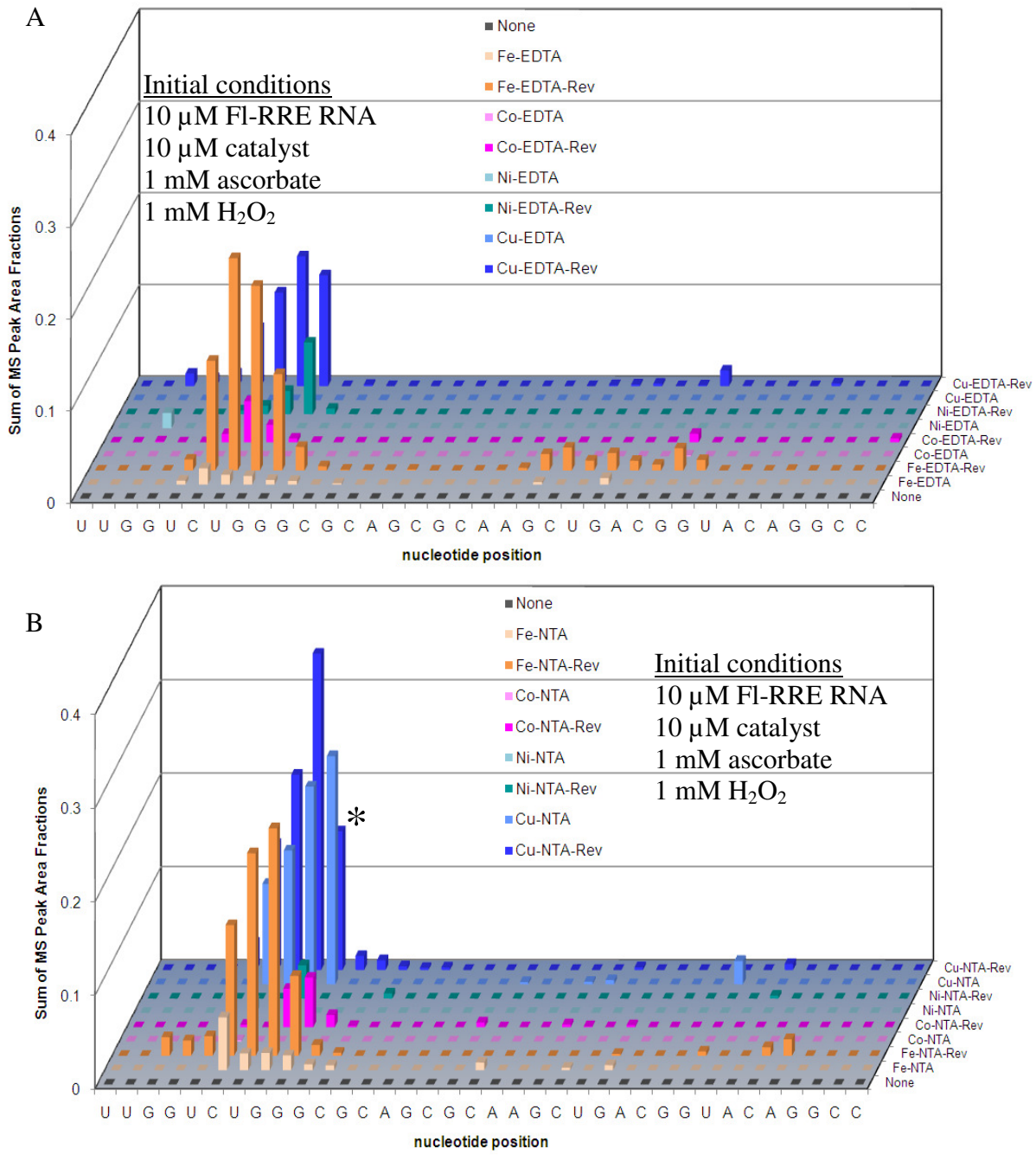

Figure SM16. Targeted cleavage of RRE RNA required attachment of catalysts to the Rev peptide in order to achieve efficient cleavage, as seen by differences in reactivity between the M-chelate-Rev catalysts and M-chelates lacking Rev. (A) M-EDTA-Rev vs M-EDTA and (B) M-NTA-Rev vs M-NTA. After 1 h incubation of each catalyst and co-reactants with the Fl-RRE RNA, the apparent abundances of individual RNA cleavage fragments were quantified. The data correspond to the abundances (MS peak area fractions) of oxidation products (cleavage fragments containing nascent terminal 3'-PO_4, 3'-PG, or 5'-PO_4 overhangs), at positions adjacent to each illustrated site of H-abstraction. * Note the exception observed for Cu-NTA (discussed later).

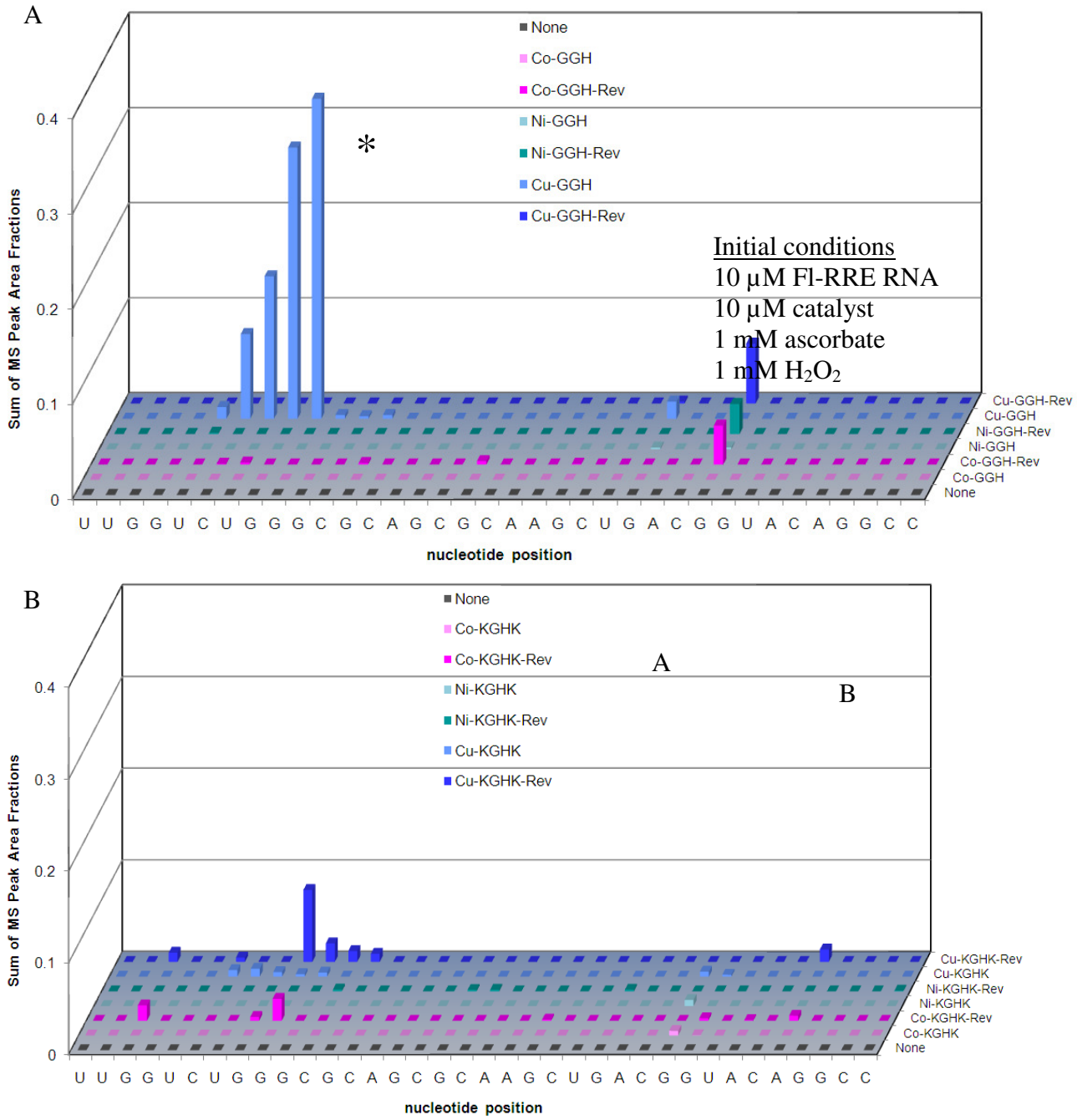

Figure SM17. Targeted cleavage of RRE RNA required attachment of catalysts to the Rev peptide in order to achieve efficient cleavage, as seen by differences in reactivity between the M-chelate-Rev catalysts and M-chelates lacking Rev. (A) M-GGH-Rev vs M-GGH and (B) M-KGHK-Rev vs M-KGHK. After 1 h incubation of each catalyst and co-reactants with the Fl-RRE RNA, the apparent abundances of individual RNA cleavage fragments were quantified. The data correspond to the abundances (MS peak area fractions) of oxidation products (cleavage fragments containing nascent terminal 3'-PO_4, 3'-PG, or 5'-PO_4 overhangs), at positions adjacent to each illustrated site of H-abstraction. * Note the exception observed for Cu-GGH (discussed later).

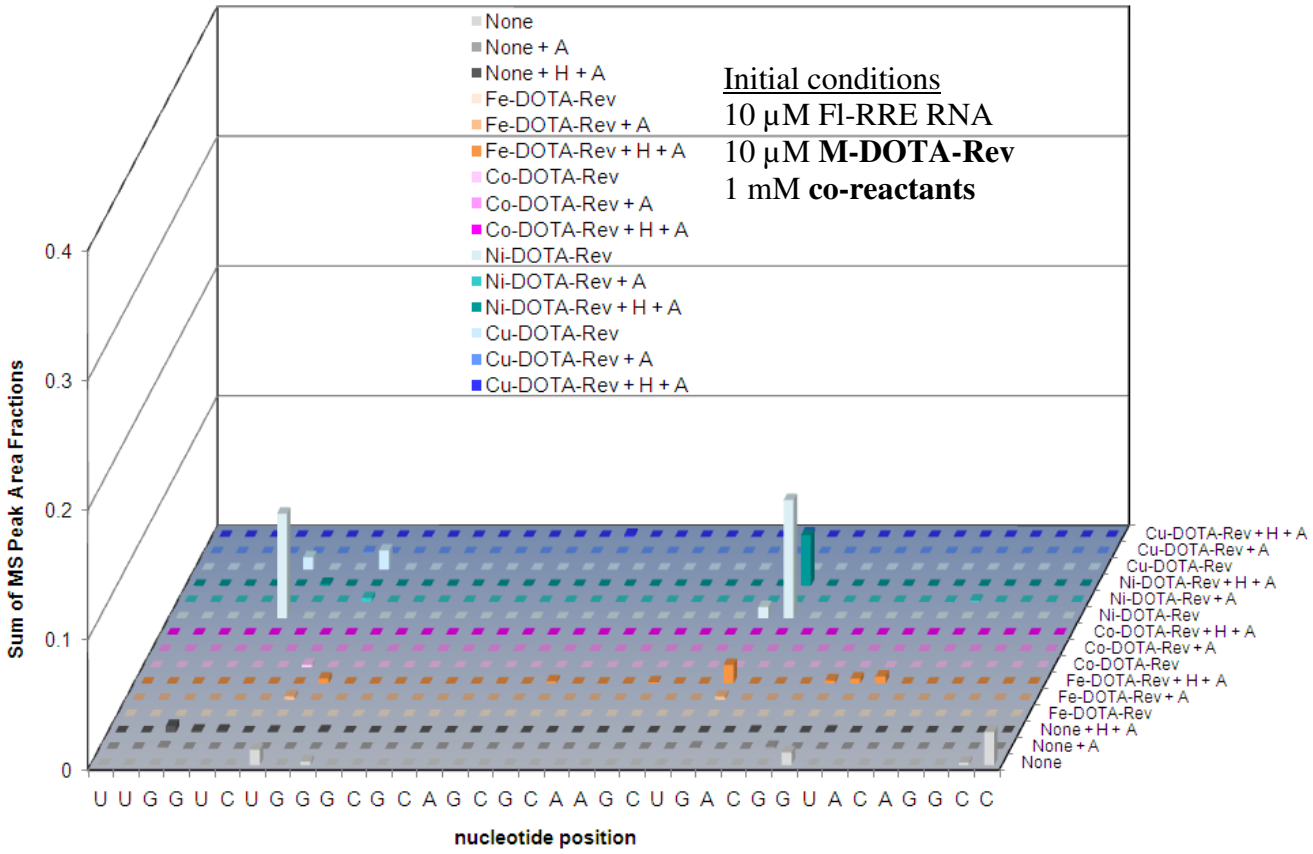

Figure SM18. Catalyst-mediated oxidative cleavage of the Fl-RRE RNA was dependent on the presence of redox co-reactants (data for M-DOTA-Rev shown here). The abundance (MS peak area fractions) of oxidation products (cleavage fragments containing nascent terminal 3'-PO_4, 3'-PG, or 5'-PO_4 overhangs at positions adjacent to each illustrated site of H-abstraction) depended on the co-reactant combinations used. Three different co-reactant combinations were used: 1 mM H_2O_2 + 1 mM ascorbate (H + A), 1 mM ascorbate (A), or no co-reactants (none).

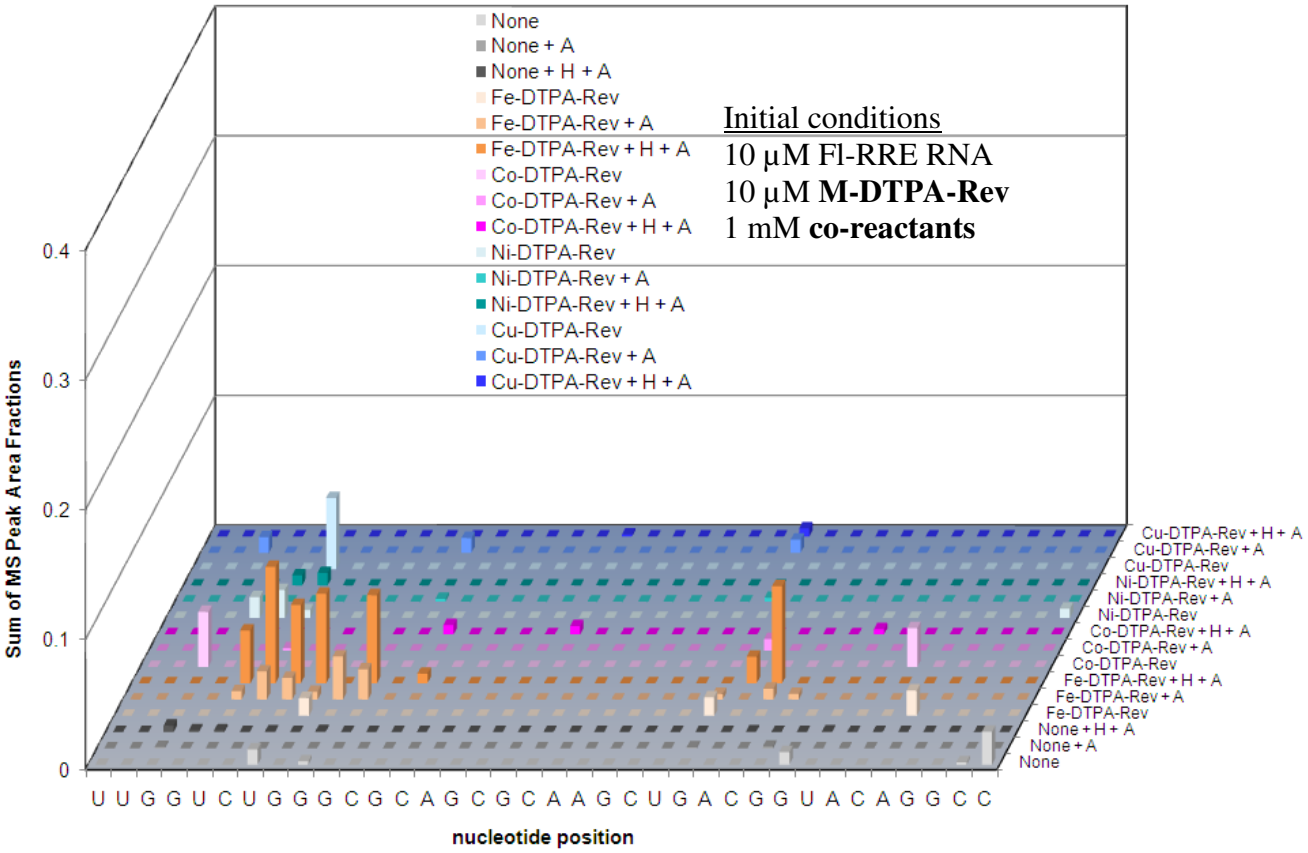

Figure SM19. Catalyst-mediated oxidative cleavage of the Fl-RRE RNA was dependent on the presence of redox co-reactants (data for M-DTPA-Rev shown here). The abundance (MS peak area fractions) of oxidation products (cleavage fragments containing nascent terminal 3'-PO_4, 3'-PG, or 5'-PO_4 overhangs at positions adjacent to each illustrated site of H-abstraction) depended on the co-reactant combinations used. Three different co-reactant combinations were used: 1 mM H_2O_2 + 1 mM ascorbate (H + A), 1 mM ascorbate (A), or no co-reactants (none).

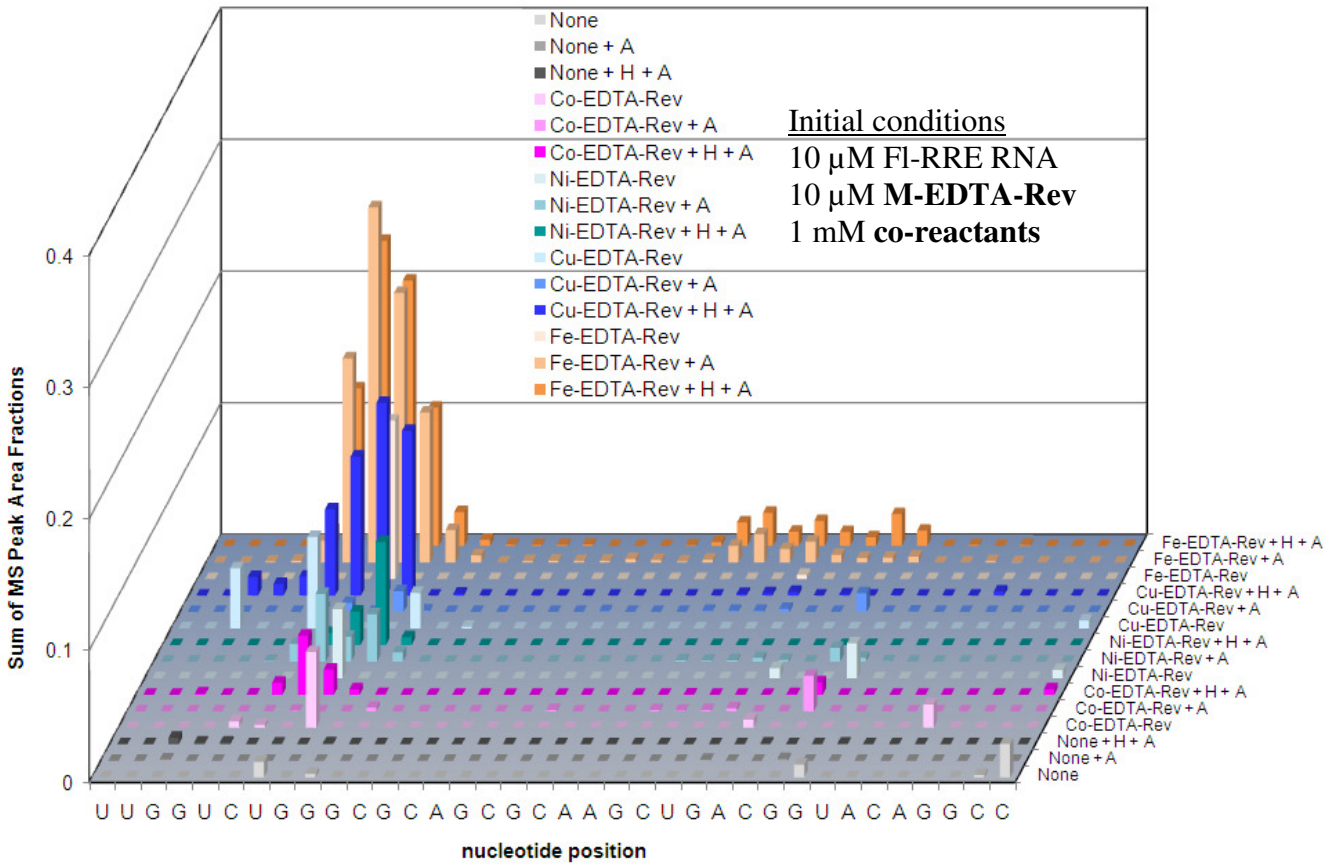

Figure SM20. Catalyst-mediated oxidative cleavage of the Fl-RRE RNA was dependent on the presence of redox co-reactants (data for M-EDTA-Rev shown here). The abundance (MS peak area fractions) of oxidation products (cleavage fragments containing nascent terminal 3'-PO_4, 3'-PG, or 5'-PO_4 overhangs at positions adjacent to each illustrated site of H-abstraction) depended on the co-reactant combinations used. Three different co-reactant combinations were used: 1 mM H_2O_2 + 1 mM ascorbate (H + A), 1 mM ascorbate (A), or no co-reactants (none).

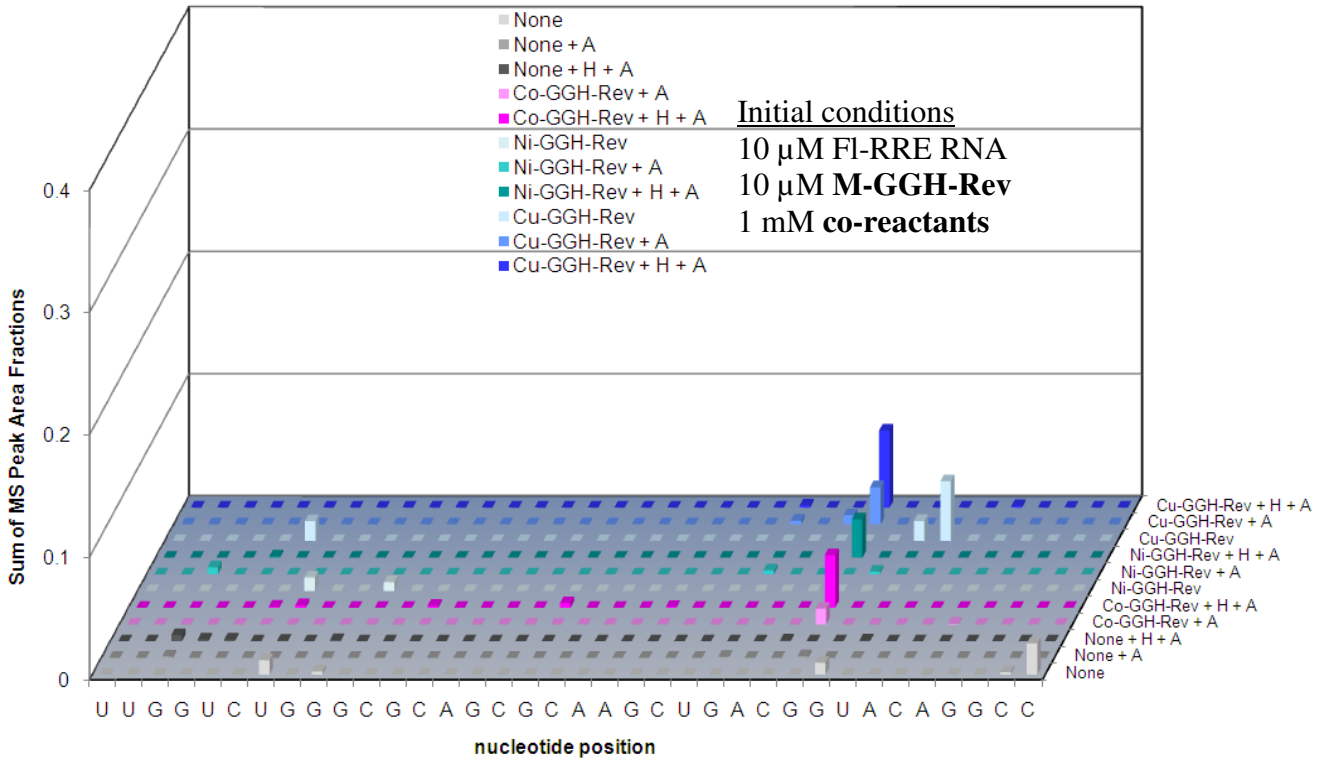

Figure SM21. Catalyst-mediated oxidative cleavage of the Fl-RRE RNA was dependent on the presence of redox co-reactants (data for M-GGH-Rev shown here). The abundance (MS peak area fractions) of oxidation products (cleavage fragments containing nascent terminal 3'-PO_4, 3'-PG, or 5'-PO_4 overhangs at positions adjacent to each illustrated site of H-abstraction) depended on the co-reactant combinations used. Three different co-reactant combinations were used: 1 mM H_2O_2 + 1 mM ascorbate (H + A), 1 mM ascorbate (A), or no co-reactants (none).

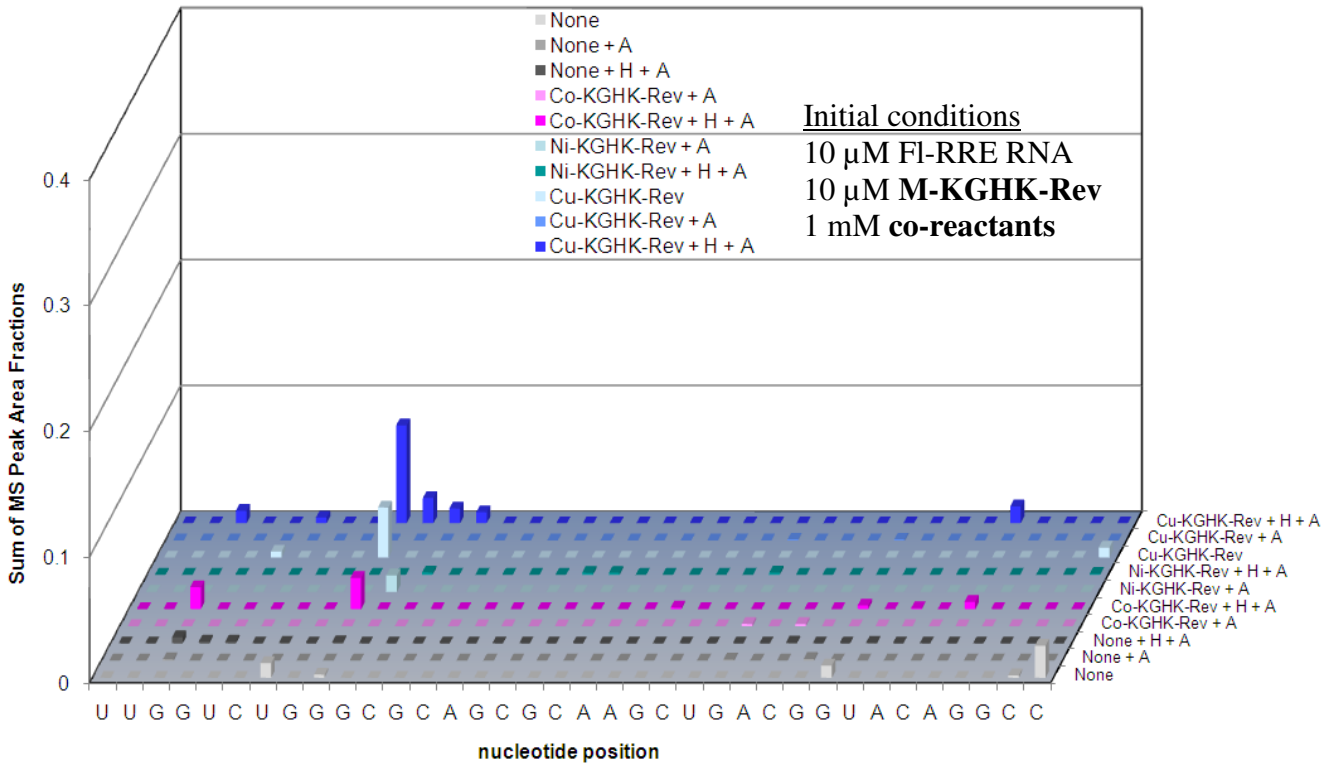

Figure SM22. Catalyst-mediated oxidative cleavage of the Fl-RRE RNA was dependent on the presence of redox co-reactants (data for M-KGHK-Rev shown here). The abundance (MS peak area fractions) of oxidation products (cleavage fragments containing nascent terminal 3'-PO_4, 3'-PG, or 5'-PO_4 overhangs at positions adjacent to each illustrated site of H-abstraction) depended on the co-reactant combinations used. Three different co-reactant combinations were used: 1 mM H_2O_2 + 1 mM ascorbate (H + A), 1 mM ascorbate (A), or no co-reactants (none).

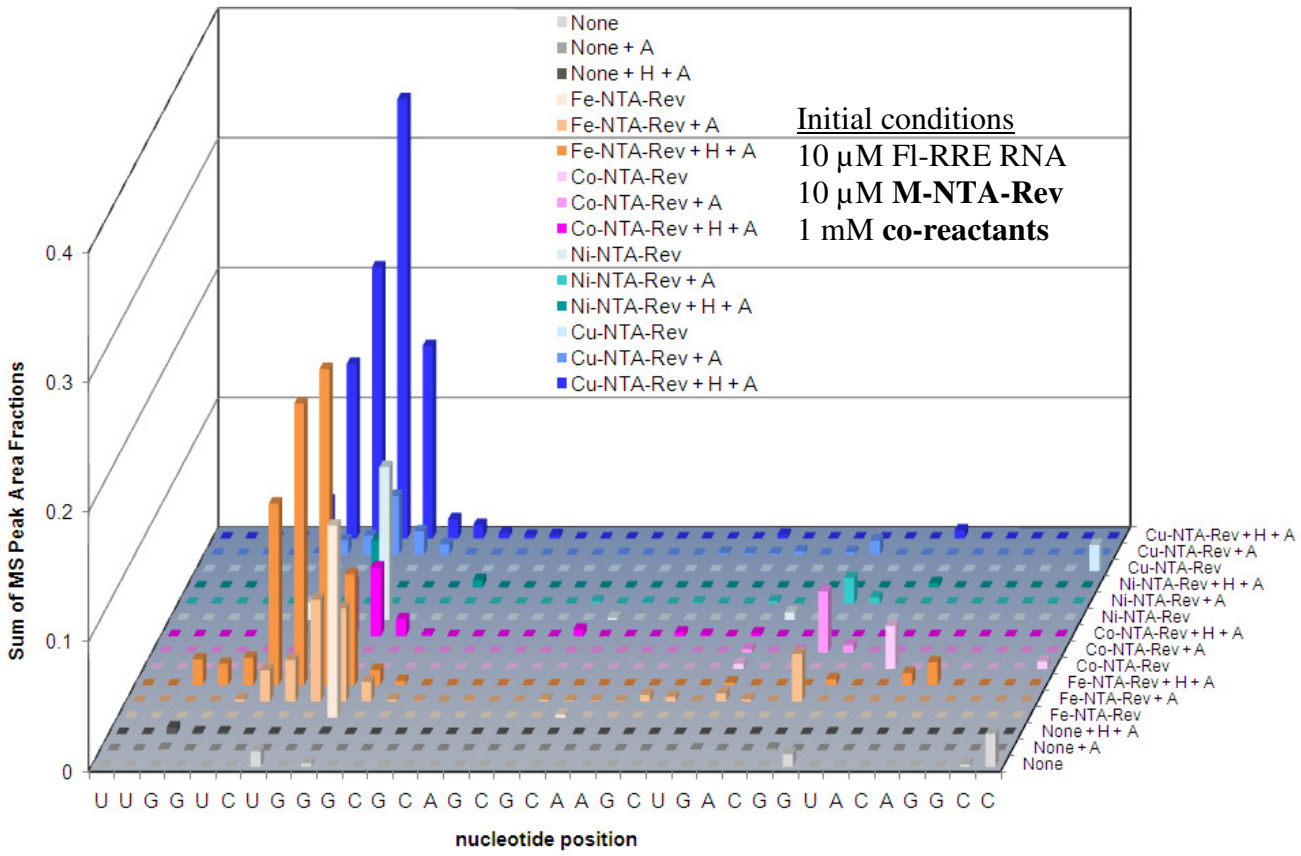

Figure SM23. Catalyst-mediated oxidative cleavage of the Fl-RRE RNA was dependent on the presence of redox co-reactants (data for M-NTA-Rev shown here). The abundance (MS peak area fractions) of oxidation products (cleavage fragments containing nascent terminal 3'-PO_4, 3'-PG, or 5'-PO_4 overhangs at positions adjacent to each illustrated site of H-abstraction) depended on the co-reactant combinations used. Three different co-reactant combinations were used: 1 mM H_2O_2 + 1 mM ascorbate (H + A), 1 mM ascorbate (A), or no co-reactants (none).

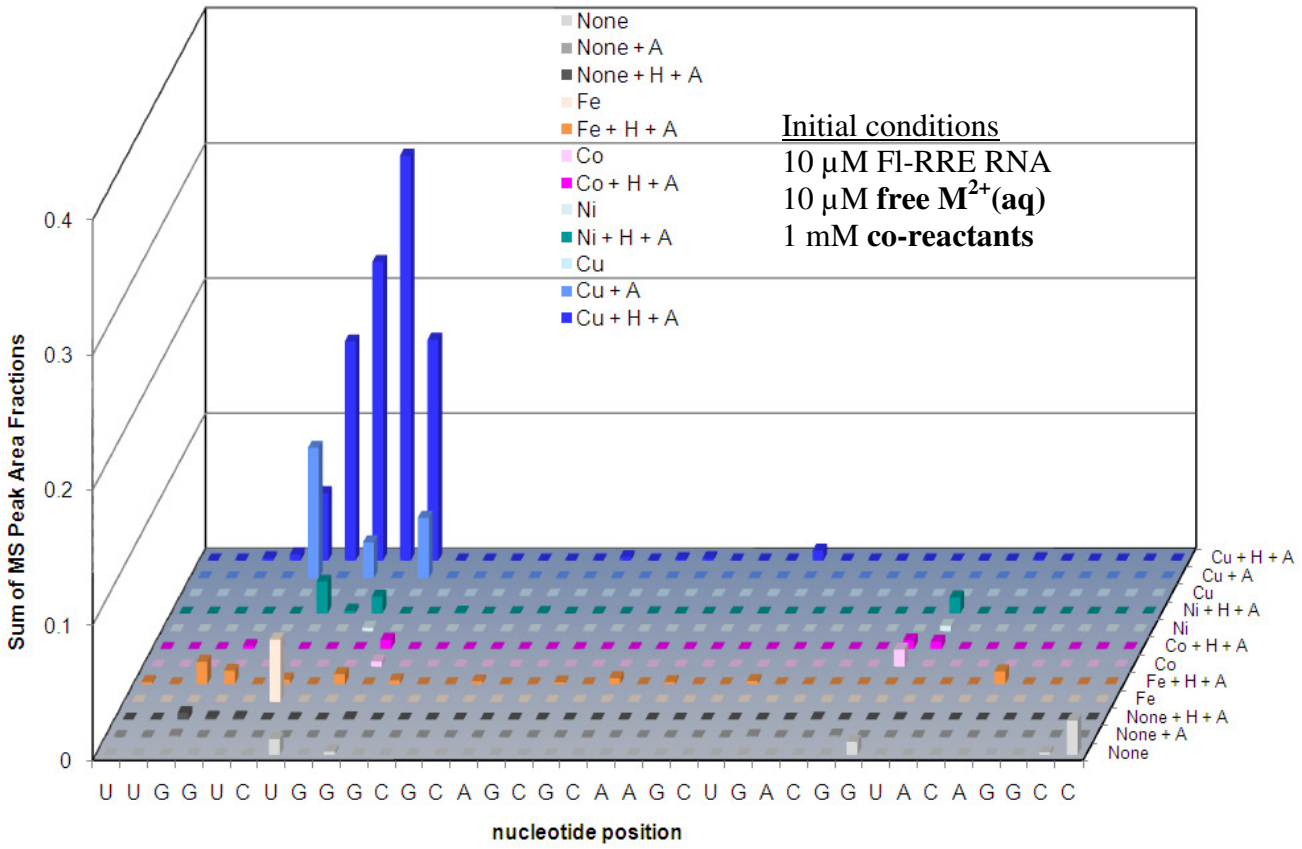

Figure SM24. Catalyst-mediated oxidative cleavage of the Fl-RRE RNA was dependent on the presence of redox co-reactants (data for free metals shown here). Among the free metals, only free Cu showed significant cleavage. The abundance (MS peak area fractions) of oxidation products (cleavage fragments containing nascent terminal 3'-PO_4, 3'-PG, or 5'-PO_4 overhangs at positions adjacent to each illustrated site of H-abstraction) depended on the co-reactant combinations used. Three different co-reactant combinations were used: 1 mM H_2O_2 + 1 mM ascorbate (H + A), 1 mM ascorbate (A), or no co-reactants (none).

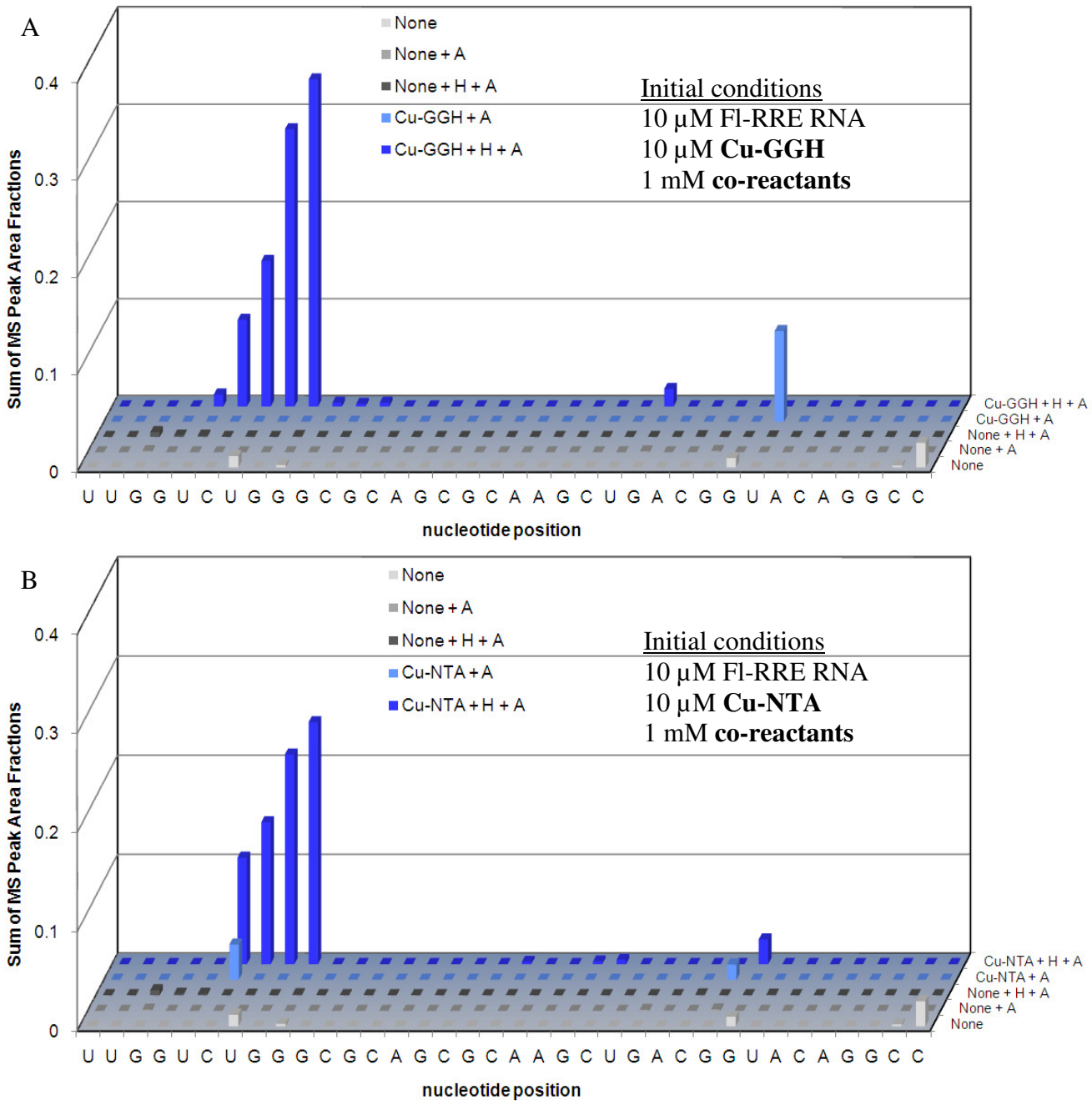

Figure SM25. Catalyst-mediated oxidative cleavage of the Fl-RRE RNA was dependent on the presence of redox co-reactants. Data for the Cu-GGH (A) and Cu-NTA (B) exceptions are shown here. The abundance (MS peak area fractions) of oxidation products (cleavage fragments containing nascent terminal 3'-PO_4, 3'-PG, or 5'-PO_4 overhangs at positions adjacent to each illustrated site of H-abstraction) depended on the co-reactant combinations used. Three different co-reactant combinations were used: 1 mM H_2O_2 + 1 mM ascorbate (H + A), 1 mM ascorbate (A), or no co-reactants (none).

NON-TARGETED BINDING AND CLEAVAGE OF RRE RNA BY FREE Cu, Cu-GGH, and Cu-NTA

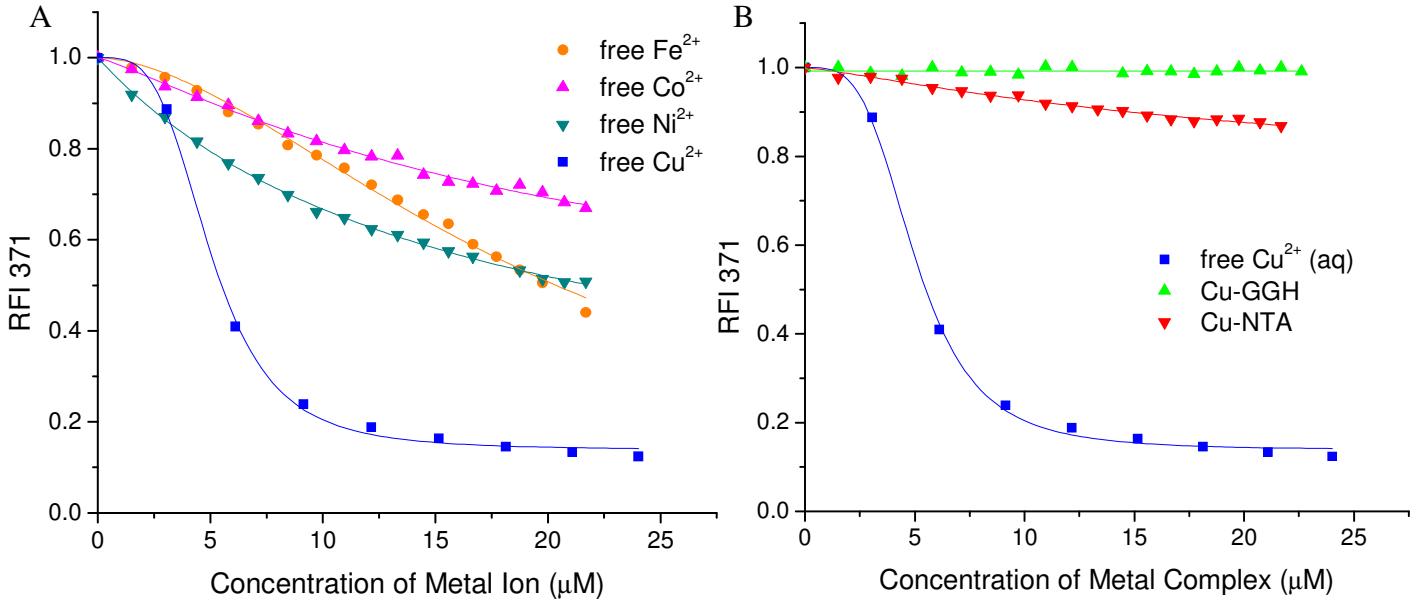

C

Complex	Fitted $K_{D,app}$ (μM)	Fitted Cooperativity (n)
free Fe^{2+}	20 ± 1	1.7 ± 0.1
free Co^{2+}	21 ± 7	1.1 ± 0.1
free Ni^{2+}	16 ± 2	1.0 ± 0.1
free Cu^{2+}	5.0 ± 0.1	3.6 ± 0.2
Cu-NTA	20 ± 10	1.2 ± 0.2
Cu-GGH	No Binding Observed	

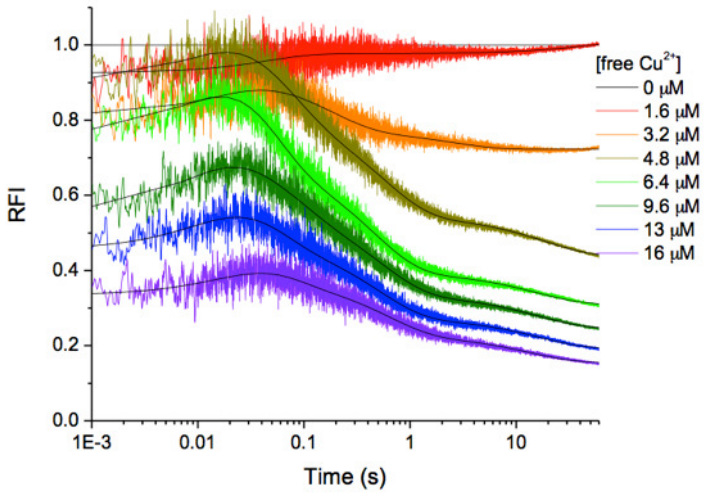

Figure SM26. The bulge of stem loop IIB of RRE RNA contains at least one low-affinity binding site for free Cu^{2+}(aq) and coordinatively-unsaturated Cu-complexes. (A) Fluorescence-monitored titrations of free metal ions into 2-aminopurine-labeled RRE RNA (AP-RRE),[3] (B) fluorescence-monitored titrations of free Cu^{2+} (aq), Cu-GGH, and Cu-NTA into AP-RRE, (C) apparent dissociation constants and fitted cooperativity values for binding to AP-RRE, and (D) stopped-flow-monitored binding of free Cu^{2+} to AP-RRE. Binding of AP-RRE by free Cu^{2+}(aq) appeared to occur with high cooperativity, with apparent binding of multiple Cu^{2+} ions to each AP-RRE molecule. This cooperativity of Cu-binding is supported by stopped-flow analysis of the kinetics of Cu^{2+} binding to AP-RRE (fit to pentaphasic first order kinetic model), which revealed five discreet events during the binding interaction and suggests initial binding of Cu^{2+} to at least one site distant from the 2-aminopurine probe (2-AP), with subsequent cooperative binding of Cu^{2+} near the 2-AP probe. Relative to free Cu^{2+}, lower-affinity binding was observed for Cu-NTA, free Fe^{2+}, free Co^{2+}, and free Ni^{2+}. Although no binding was directly observed for Cu-GGH upon titration into AP-RRE, it is likely that the Cu-GGH binds in a manner that does not alter the fluorescence of the AP probe. AP-RRE fluorescence emission was monitored at 371 nm (an emission filter with 360 nm cutoff was used for stopped-flow analysis), with excitation at 310 nm.

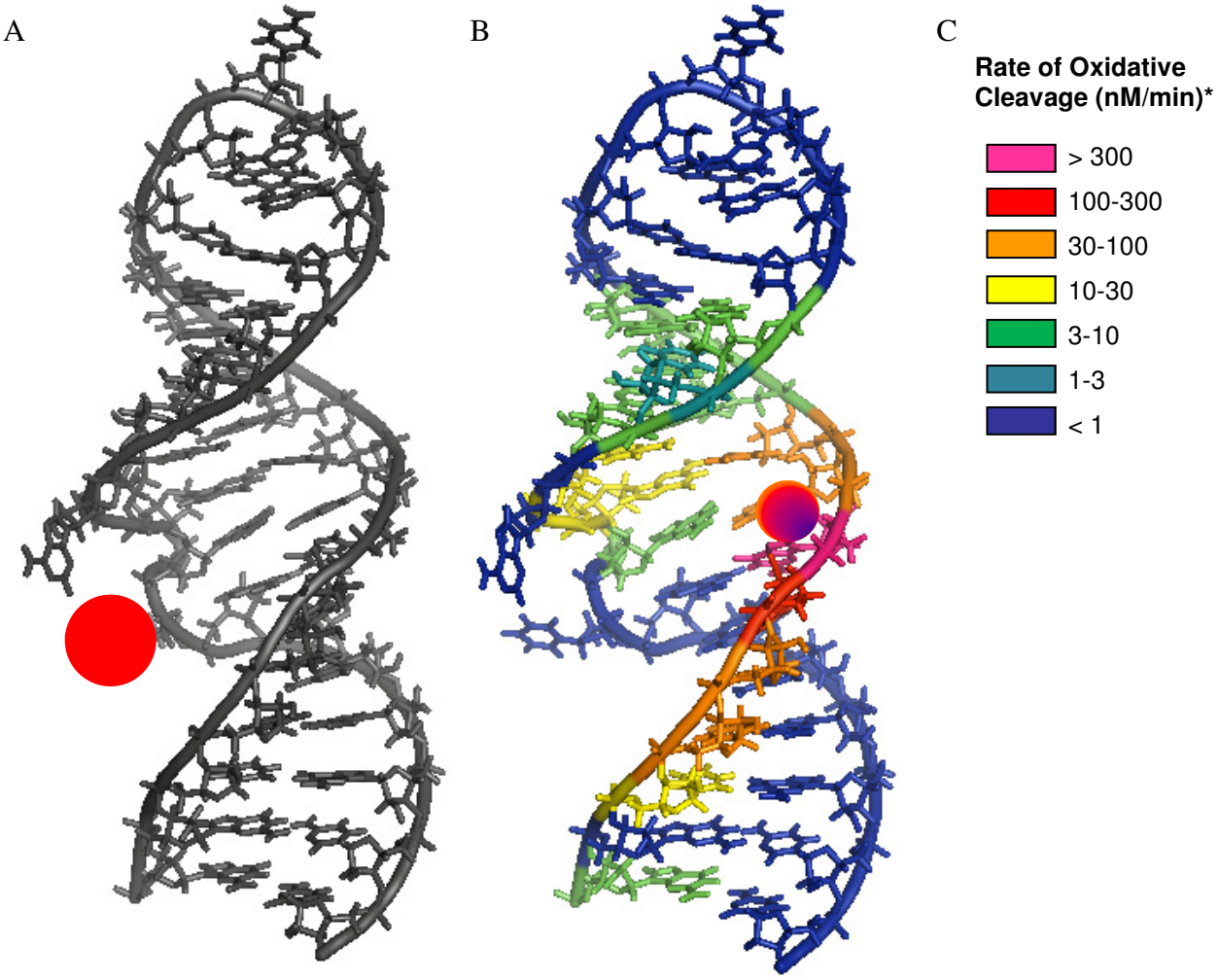

Figure SM27. (A) Location of the 2-aminopurine label in AP-RRE (red circle). (B) The binding site(s) for free Cu^{2+}(aq) can be predicted based on the apparent initial rates (color-coded) of oxidative cleavage of RRE RNA by free Cu^{2+}(aq) and co-reactants at each nucleotide position within the RRE RNA. A predicted Cu-binding site is shown (approximately) by the purple sphere. (C) Color-code (log scale) for apparent initial rates of oxidative scission (sum of initial rates of formation of cleavage fragments containing nascent terminal 3'-PO_4, 3'-PG, or 5'-PO_4 overhangs). The relatively high activity of free Cu^{2+}(aq) and the Cu-GGH and Cu-NTA chelates lacking Rev was the result of the combination of a low-affinity Cu-binding site within the RRE RNA (discussed above) and the high concentrations of catalyst and RNA required for MALDI-TOF MS detection (10 μM). Unlike the other Cu-chelates used, the Cu-GGH and Cu-NTA chelates are similar to free Cu^{2+}(aq) in that at least two non-chelated coordination sites are present.

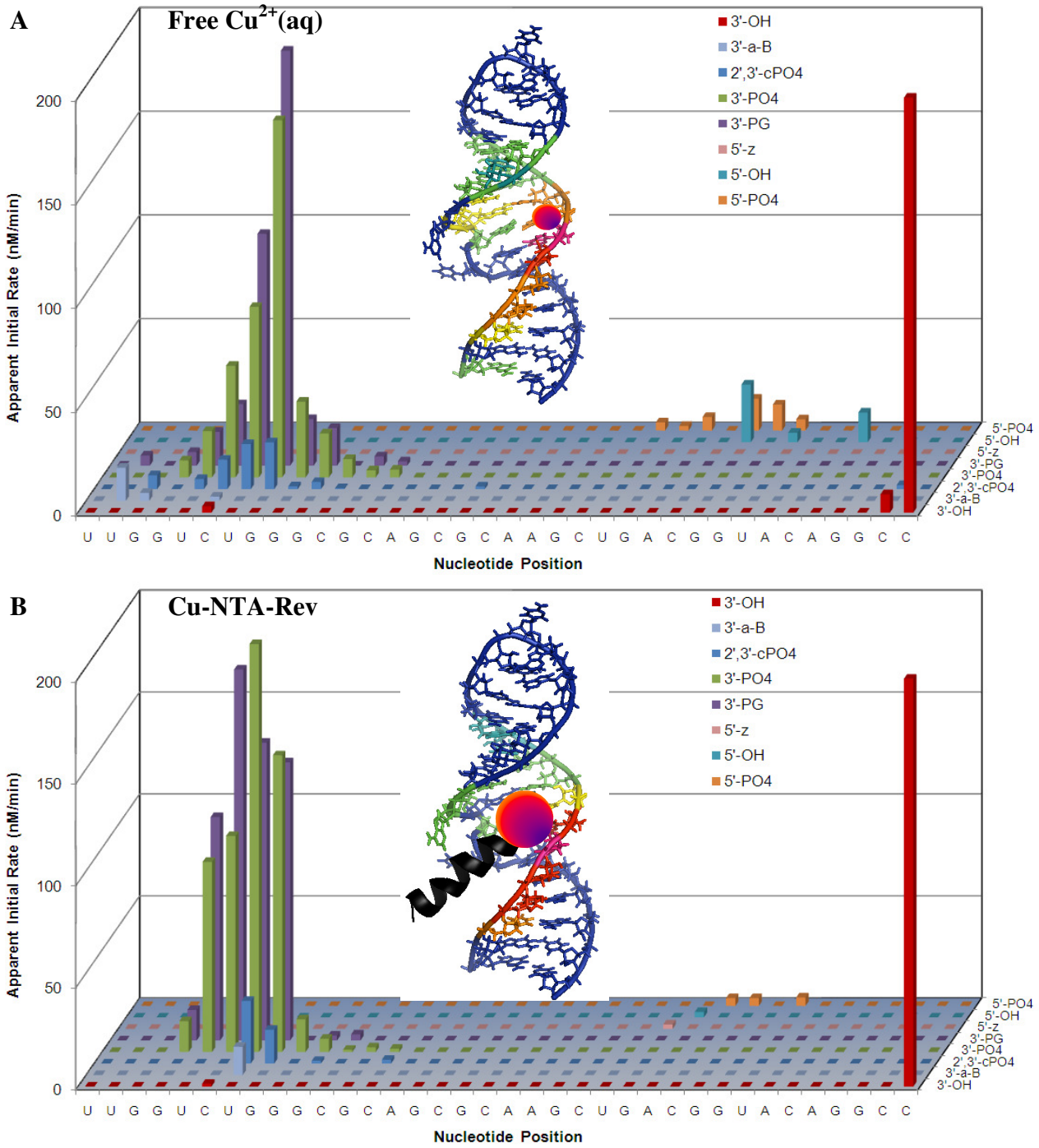

Figure SM28. The distribution of cleavage sites/rates is distinct for free Cu^{2+}(aq) vs M-chelate-Rev catalysts. (A) Apparent initial rates of formation of cleavage products for free Cu^{2+}(aq) and co-reactants. (B) Apparent initial rates of formation of cleavage products for Cu-NTA-Rev and co-reactants. The relatively high activity of free Cu^{2+}(aq) and the Cu-GGH and Cu-NTA chelates lacking Rev was the result of the combination of a low-affinity Cu-binding site within the RRE RNA (discussed above) and the high concentrations of catalyst and RNA required for MALDI-TOF MS detection (10 μM).

CHARACTERIZATION OF THE FLUORESCENT 2-HYDROXYPROPENE-BIS(THIOBARBITURIC ACID) ADDUCT

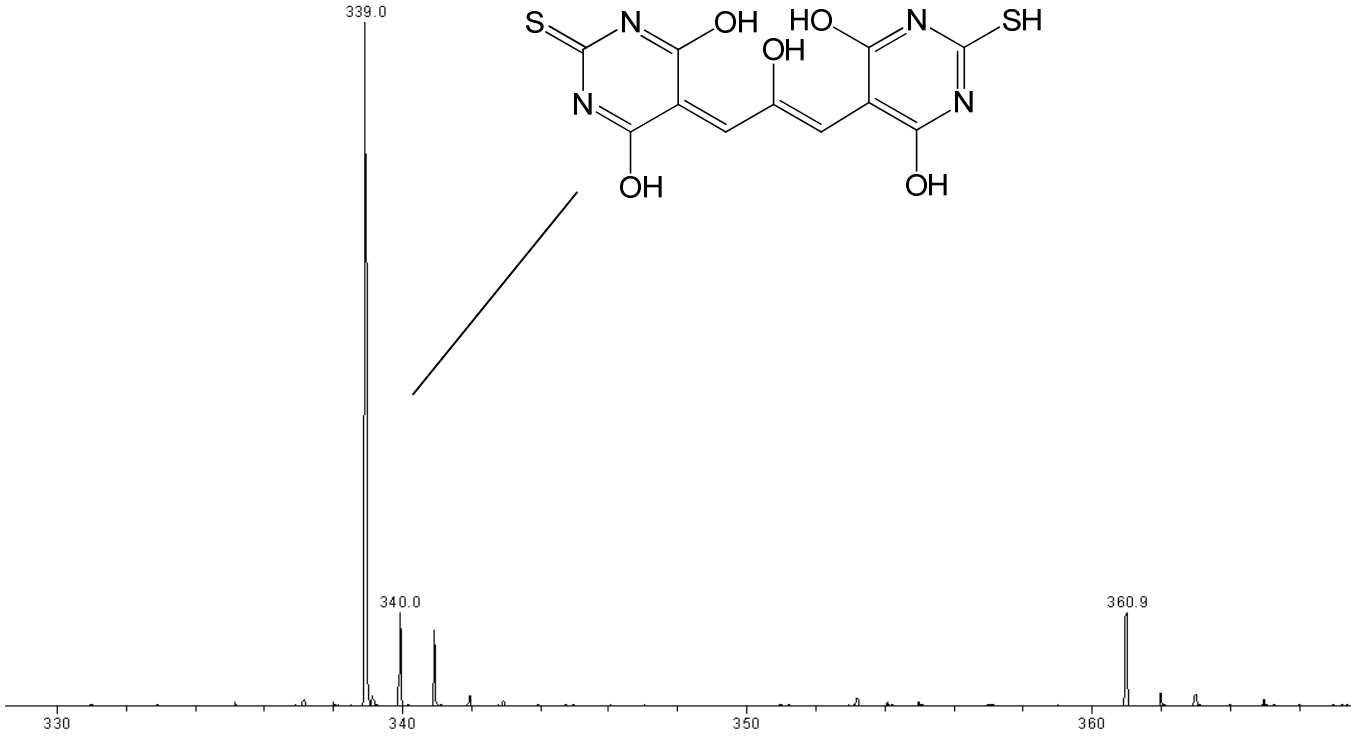

Figure SM29. ESI-MS confirmation of formation of the 2-hydroxypropene-bis(thiobarbituric acid) adduct (ESI-MS performed in negative ion mode). The peak at 339 amu is [adduct - 1H]$^{1-}$, and the peak at 361 amu is [adduct - 2H + Na]$^{1-}$.

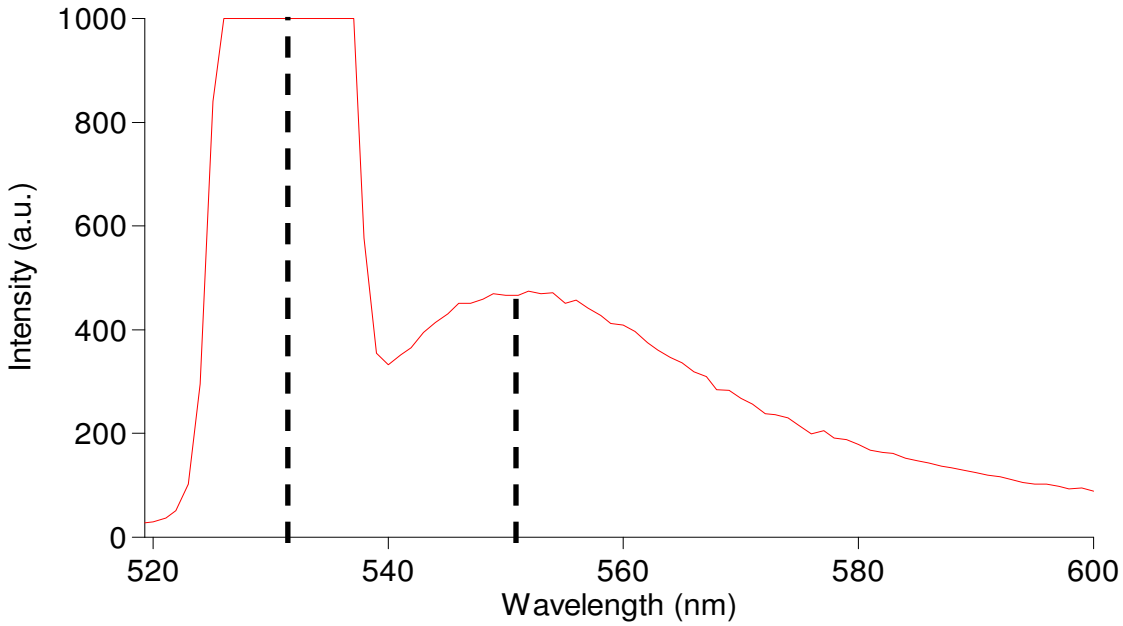

Figure SM30. Fluorescence emission of the 2-hydroxypropene-bis(thiobarbituric acid) adduct, under the same conditions as used for quantification of base 2-hydroxypropenals released following 4'-H abstraction from RNA. The protocol used for quantification of base 2-hydroxypropenals released following 4'-H abstraction from RNA is described in the manuscript; fluorescence emission at 550 nm was monitored, with excitation at 532 nm (emission and excitation wavelengths are illustrated by the dashed lines).

MASS-MATCHING DETAILS

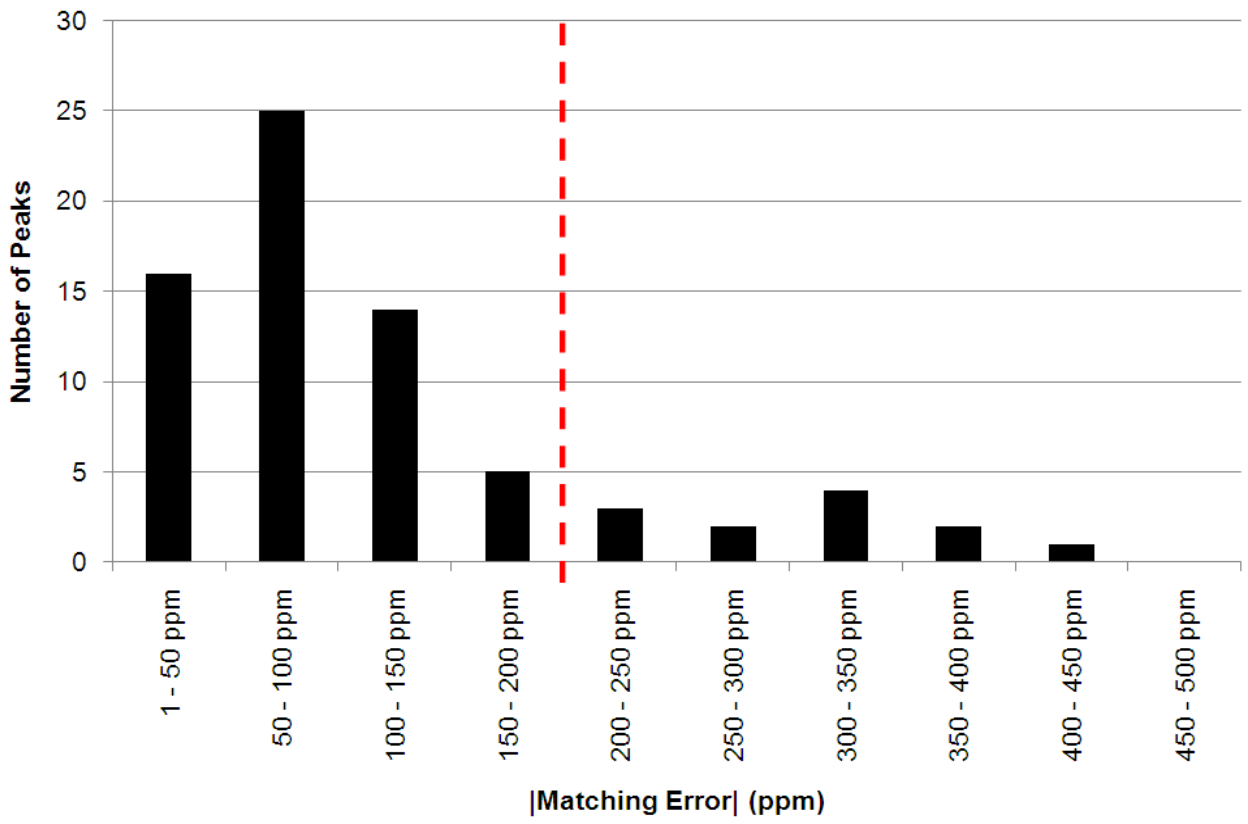

Figure SM31. Histogram showing the distribution of mass-matching errors for all assigned peaks for one reaction. Although a mass-matching tolerance of 200 ppm was used for all other data (shown by the red dashed line), the data shown in this figure were generated by use of a mass-matching tolerance of 500 ppm, in order to show the distribution of errors. When a mass-matching tolerance of 200 ppm was used, the root-mean-square (RMS) mass-matching error for the reaction was 113 ppm. The data and RMS calculation shown here are from the 120 min time point from the Fe-EDTA-Rev/RRE RNA/co-reactants reaction.

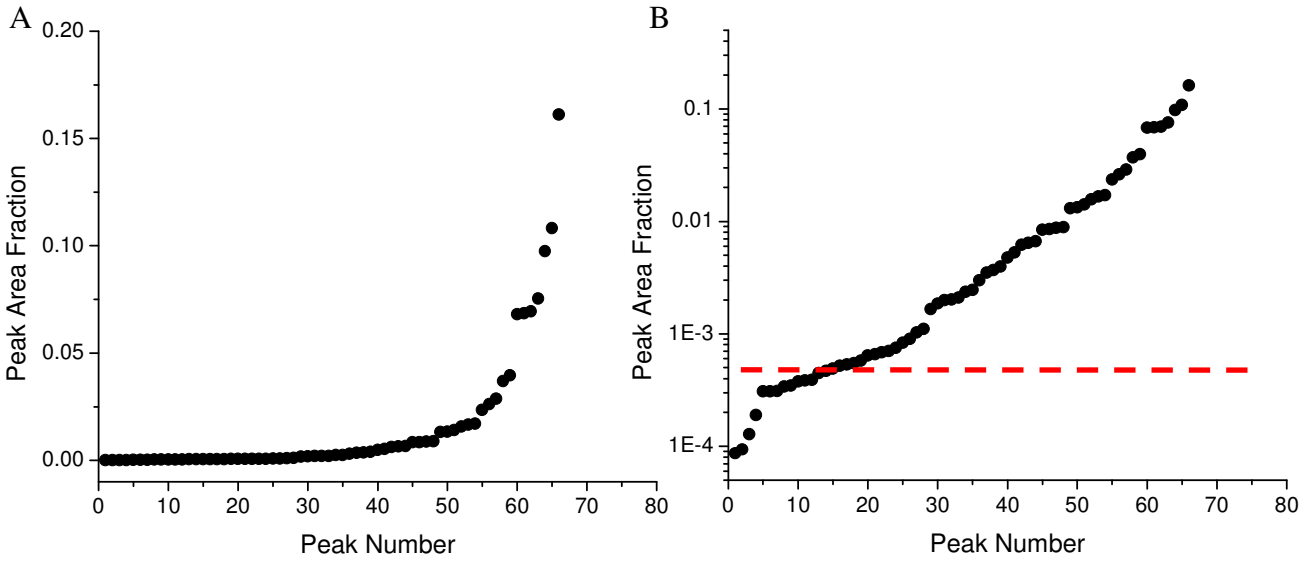

Figure SM32. In order for a MS peak to be considered 'real', the peak area fraction was required to be >0.0005, following assignment of peaks. Additionally, the m/z for an observed peak was required to be within a matching threshold (200 ppm) relative to the m/z for the predicted peak (shown elsewhere). The peaks shown here resulted from the 120 min timepoint from the Fe-EDTA-Rev/RRE RNA/coreactants reaction: (A) linear plot and (B) semi-log plot of the same data. The peak area fraction threshold of 0.0005 is represented by the red line.

Nascent 3' Overhangs								Nascent 5' Overhangs			
3'-OH		2,3-cyclic phosphate		3'-phosphate		3'-phosphoglycolate		5'-OH		5'-phosphate	
m/z (Da)	nucl. pos.	m/z (Da)	nucl. pos.	m/z (Da)	nucl. pos.	m/z (Da)	nucl. pos.	m/z (Da)	nucl. pos.	m/z (Da)	nucl. pos.
12171.52	**36**										
11866.34	35	11928.3	35	11946.32	35	12004.36	35	11327.86	2	11407.84	2
11561.16	34	11623.12	34	11641.14	34	11699.18	34	11021.7	3	11101.68	3
11215.95	33	11277.91	33	11295.93	33	11353.97	33	10676.49	4	10756.47	4
10870.74	32	10932.7	32	10950.72	32	11008.76	32	10331.28	5	10411.26	5
10541.53	31	10603.49	31	10621.51	31	10679.55	31	10025.11	6	10105.09	6
10236.35	30	10298.31	30	10316.33	30	10374.37	30	9719.93	7	9799.91	7
9907.14	29	9969.1	29	9987.12	29	10045.16	29	9413.76	8	9493.74	8
9600.97	28	9662.93	28	9680.95	28	9738.99	28	9068.55	9	9148.53	9
9255.76	27	9317.72	27	9335.74	27	9393.78	27	8723.34	10	8803.32	10
8910.55	26	8972.51	26	8990.53	26	9048.57	26	8378.13	11	8458.11	11
8605.37	25	8667.33	25	8685.35	25	8743.39	25	8072.95	12	8152.93	12
8276.16	24	8338.12	24	8356.14	24	8414.18	24	7727.74	13	7807.72	13
7930.95	23	7992.91	23	8010.93	23	8068.97	23	7422.56	14	7502.54	14
7624.78	22	7686.74	22	7704.76	22	7762.8	22	7093.35	15	7173.33	15
7319.6	21	7381.56	21	7399.58	21	7457.62	21	6748.14	16	6828.12	16
6974.39	20	7036.35	20	7054.37	20	7112.41	20	6442.96	17	6522.94	17
6645.18	19	6707.14	19	6725.16	19	6783.2	19	6097.75	18	6177.73	18
6315.97	18	6377.93	18	6395.95	18	6453.99	18	**5792.57**	**19**	5872.55	19
6010.79	17	6072.75	17	6090.77	17	6148.81	17	5463.36	20	5543.34	20
5665.58	16	5727.54	16	5745.56	16	5803.6	16	5134.15	21	5214.13	21
5360.39	15	5422.35	15	5440.37	15	5498.41	15	4788.94	22	4868.92	22
5015.18	14	5077.14	14	5095.16	14	5153.2	14	4483.76	23	4563.74	23
4685.97	13	**4747.93**	**13**	4765.95	13	4823.99	13	4177.59	24	4257.57	24
4380.79	12	4442.75	12	4460.77	12	4518.81	12	3832.38	25	3912.36	25
4035.58	11	4097.54	11	4115.56	11	4173.6	11	3503.17	26	3583.15	26
3730.4	10	3792.36	10	3810.38	10	3868.42	10	3197.99	27	3277.97	27
3385.19	9	3447.15	9	3465.17	9	3523.21	9	2852.78	28	2932.76	28
3039.98	8	**3101.94**	**8**	3119.96	8	3178	8	2507.57	29	2587.55	29
2694.77	7	**2756.73**	**7**	2774.75	7	2832.79	7	**2201.4**	**30**	2281.38	30
2388.6	6	**2450.56**	**6**	2468.58	6	2526.62	6	1872.19	31	1952.17	31
2083.42	5	**2145.38**	**5**	2163.4	5	2221.44	5	**1567.01**	**32**	1646.99	32
1777.25	4	1839.21	4	1857.23	4	1915.27	4	1237.8	33	1317.78	33
1432.04	3	**1494**	**3**	1512.02	3	1570.06	3	892.59	34	972.57	34
1086.83	2	1148.79	2	1166.81	2	1224.85	2	547.38	35	627.36	35
780.66	1	842.62	1	860.64	1	918.68	1	242.2	36	322.18	36

Table SM3. Predicted masses for products ions (z = -1) resulting from cleavage of Fl-RRE RNA (36-mer). The predicted masses shown here correspond to $[RNA]^{1-}$ fragments terminated with one of the listed nascent overhangs, at one of the positions shown. These masses were used for assignment of peaks in mass spectra. All fragments with nascent 3' overhangs were terminated at the 5' end with fluorescein; all fragments with nascent 5' overhangs were terminated at the 3' end with a 3'-hydroxyl group. The Fl-RRE RNA is similarly terminated at the 5' end with fluorescein and at the 3' end with a 3'-hydroxyl group (unreacted; m/z = 12171.53 Da). Peaks used for internal calibration are shown in bold (also included $[Fl\text{-}RRE - 2H]^{2-}$ with m/z = 6085.26 Da).

CONCENTRATION-DEPENDENCE

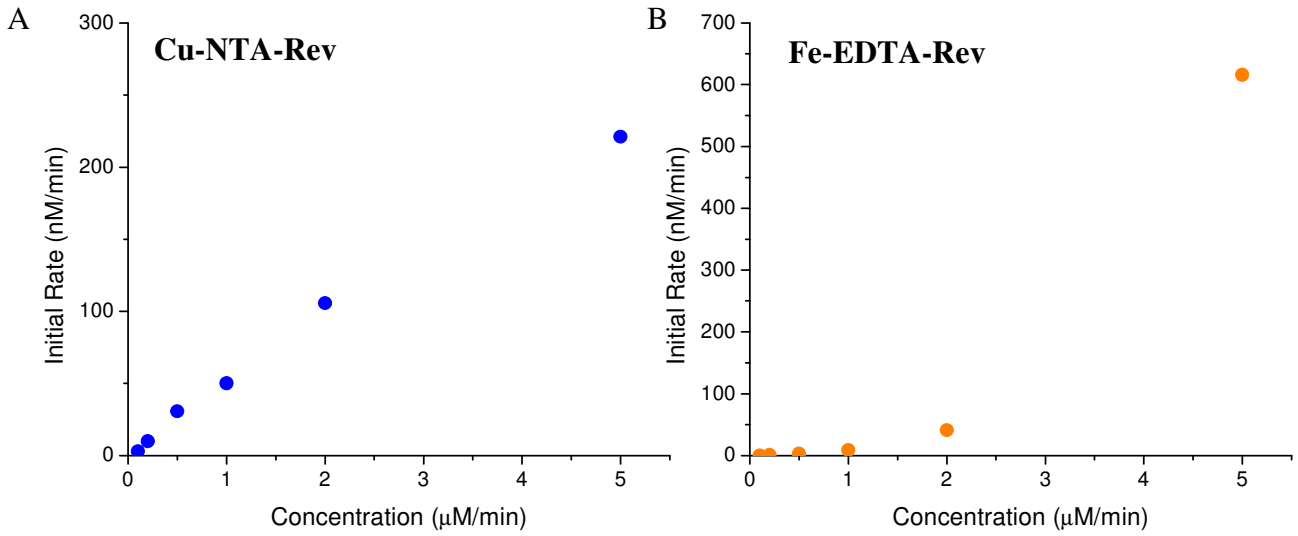

C

$$M^{2+} + H_2O_2 \xrightarrow{k_1} OH^- + OH\bullet + M^{3+}$$

$$AscH + M^{3+} \xrightarrow{k_2} M^{2+} + Asc\bullet^- + 2H^+$$

$$OH\bullet + RNA \xrightarrow{k_3} H_2O + RNA^*$$

$$Scavenger + OH\bullet \xrightarrow{k_S} Scavenger\bullet + H_2O$$

Assuming steady-state concentration of OH•, the rate law is:

$$Rate = \frac{k_1 k_3 [M^{2+}][H_2O_2][RNA]}{k_3[RNA] + k_S[scavenger]}$$

Figure SM33. Dependence of the initial rate of RNA cleavage on the concentration of the complex between Fl-RRE RNA and the catalyst (A) Cu-NTA-Rev or (B) Fe-EDTA-Rev. The concentration of each catalyst:RNA complex (1:1) was varied, while the initial concentrations of H_2O_2 and ascorbate were fixed at 1 mM, and time-dependent incubations were performed. Disappearance of full-length 5'-fluorescein end-labeled RRE RNA was monitored by PAGE analysis, and initial rates were determined by fitting to a first order model. The data show profiles that are consistent with a higher susceptibility to scavenging of ROS at lower concentrations of Fe-EDTA-Rev/RNA, but not for Cu-NTA-Rev/RNA. (C) Proposed rate law for cleavage of RNA by a M-chelate-Rev catalyst (M), in the presence of the co-reactants ascorbate (AscH) and H_2O_2, assuming a rapid equilibration to a steady-state concentration of hydroxyl radical as the reactive intermediate. The k_S[scavenger] term in the denominator is likely to be larger if RNA cleavage is mediated by a metal-dissociated hydroxyl radical, relative to a metal-associated hydroxyl radical, since a metal-dissociated radical has a higher susceptibility to scavenging. A large k_S[scavenger] term is expected to result in a lag phase in the concentration dependence plots shown above. Cleavage by Fe-EDTA-Rev is most likely mediated by a metal-dissociated ROS (large k_S[scavenger] term). Cleavage by Cu-NTA-Rev is most likely mediated by a metal-associated ROS (small k_S[scavenger] term).

Complex	Initial Rate of Cleavage of Fl-RRE with Differing Concentrations of M-chelate-Rev / Fl-RRE	
	Conc. = 10 μM [a]	Conc. = 0.1 μM [1]
Fe-DOTA-Rev	8 ± 2	0.026 ± 0.006
Fe-DTPA-Rev	190 ± 40	0.16 ± 0.04
Fe-EDTA-Rev	4000 ± 1000	0.00 ± 0.02
Fe-NTA-Rev	250 ± 40	0.031 ± 0.006
Co-DOTA-Rev	< 4	0.063 ± 0.005
Co-DTPA-Rev	n.d.	0.063 ± 0.007
Co-EDTA-Rev	6 ± 1	0.17 ± 0.03
Co-GGH-Rev	n.d.	0.003 ± 0.007
Co-KGHK-Rev	< 11	0.031 ± 0.003
Co-NTA-Rev	6 ± 2	0.069 ± 0.003
Ni-DOTA-Rev	8 ± 2	0.009 ± 0.008
Ni-DTPA-Rev	n.d.	0.054 ± 0.008
Ni-EDTA-Rev	32 ± 6	0.18 ± 0.05
Ni-GGH-Rev	n.d.	0.026 ± 0.005
Ni-KGHK-Rev	< 15	0.043 ± 0.003
Ni-NTA-Rev	90 ± 20	0.067 ± 0.005
Cu-DOTA-Rev	4 ± 3	0.8 ± 0.1
Cu-DTPA-Rev	n.d.	0.496 ± 0.008
Cu-EDTA-Rev	46 ± 5	0.14 ± 0.03
Cu-GGH-Rev	n.d.	0.045 ± 0.005
Cu-KGHK-Rev	80 ± 50	0.060 ± 0.005
Cu-NTA-Rev	300 ± 30	2.1 ± 0.2
None	< 4	0.015 ± 0.005

Table SM4. Dependence of the initial rate of RNA cleavage on the concentration of the complex between Fl-RRE RNA and each catalyst. The concentration of each catalyst:RNA complex (1:1) was varied (10 and 0.1 μM), while the initial concentrations of H_2O_2 and ascorbate were fixed at 1 mM, and time-dependent incubations were performed. Disappearance of full-length 5'-fluorescein end-labeled RRE RNA was monitored by PAGE analysis, and initial rates were determined by fitting to a first order model. n.d. = not determined. [a] This study.

ADDITIONAL MECHANISMS

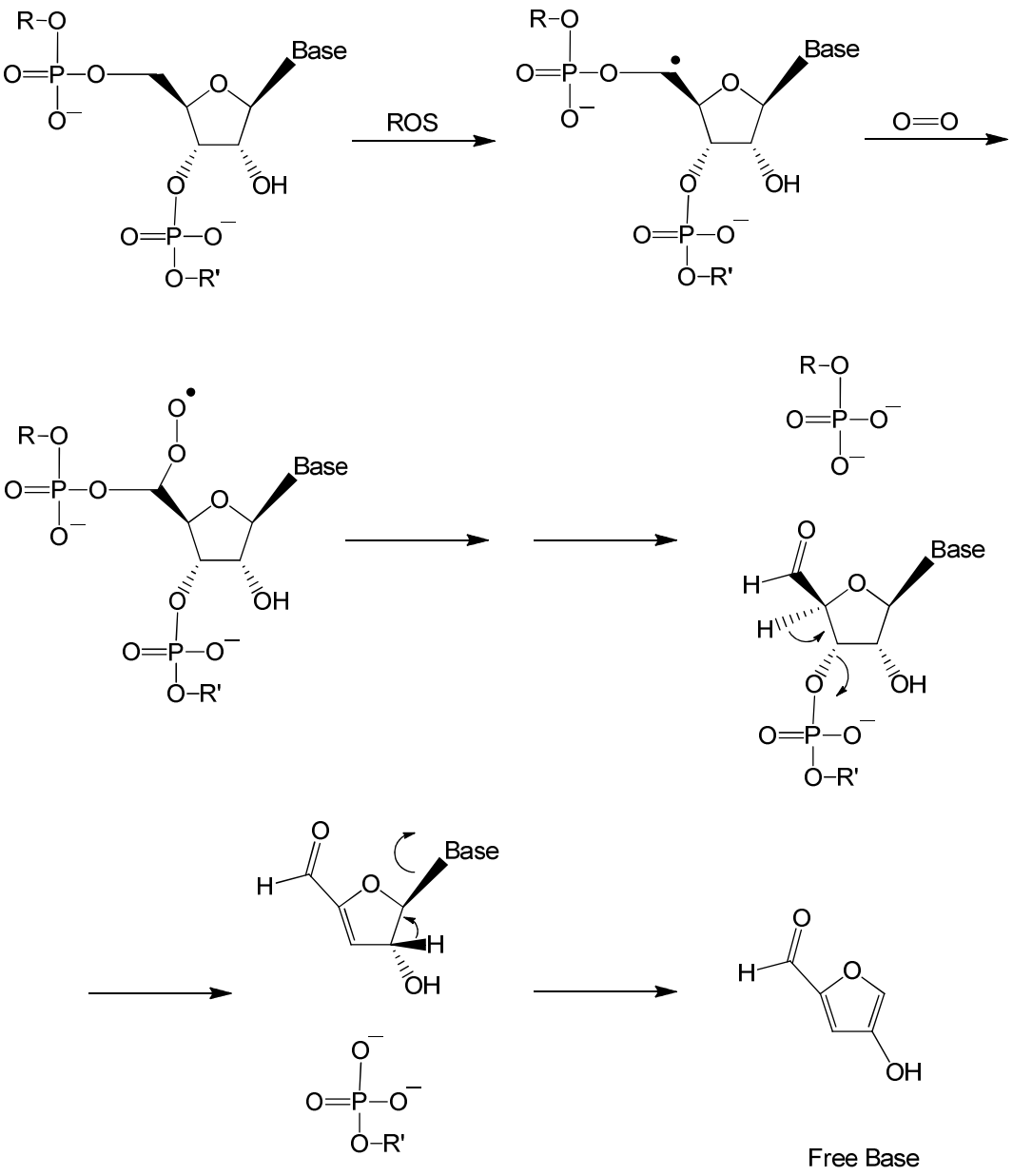

Figure SM34. Proposed mechanism for **5'-H abstraction mediated by ROS** generated by catalytic metal centers under aerobic conditions, observed by formation of 3'-phosphate products. The last two steps require additional heating. Slight mechanistic variations are possible that give the same RNA fragments.

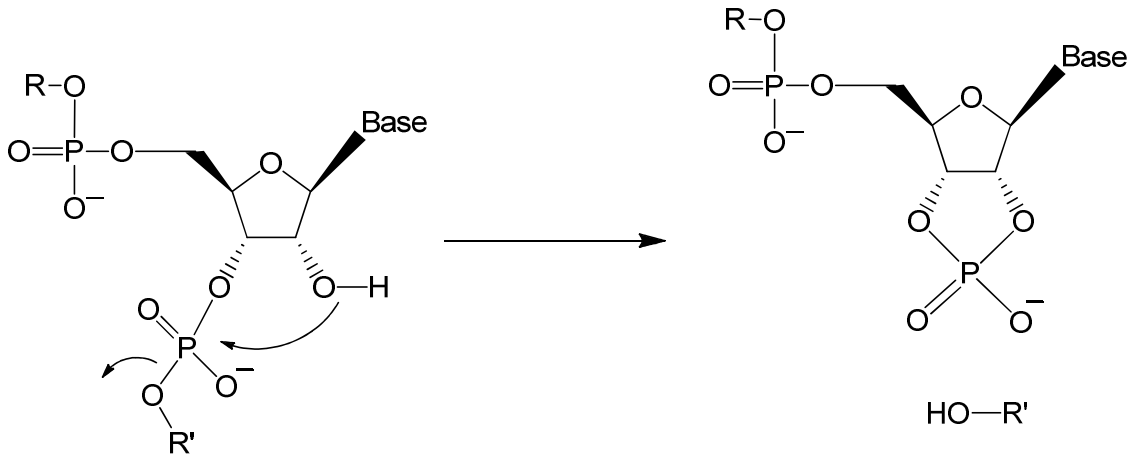

Figure SM35. Proposed mechanism for **2'-OH-mediated endonucleolytic cleavage** of RNA to give fragments containing nascent 2',3'-cyclic phosphate or 5'-hydroxyl termini (c-fragments or y-fragments, respectively).

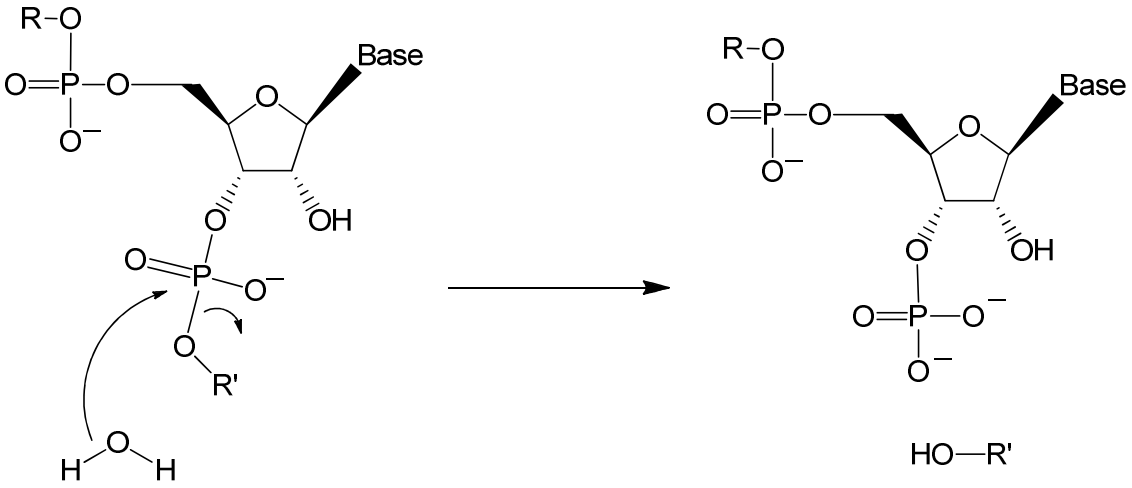

Figure SM36. Proposed mechanism for possible **hydrolysis** of RNA to give fragments containing nascent 3'-phosphate and 5'-hydroxyl termini (d-fragments and y-fragments, respectively). The mechanism may involve a 2',3'-cyclic phosphate intermediate, if the reaction occurs by 2'-OH-mediated attack; if this occurs, a 2'-phosphate is expected to result, in approximately equal abundance to the 3'-phosphate. It is also possible for hydrolysis to give fragments containing nascent 5'-phosphate and 3'-hydroxyl termini, depending on which P-O bond is hydrolyzed.

MISCELLANEOUS ANALYSES

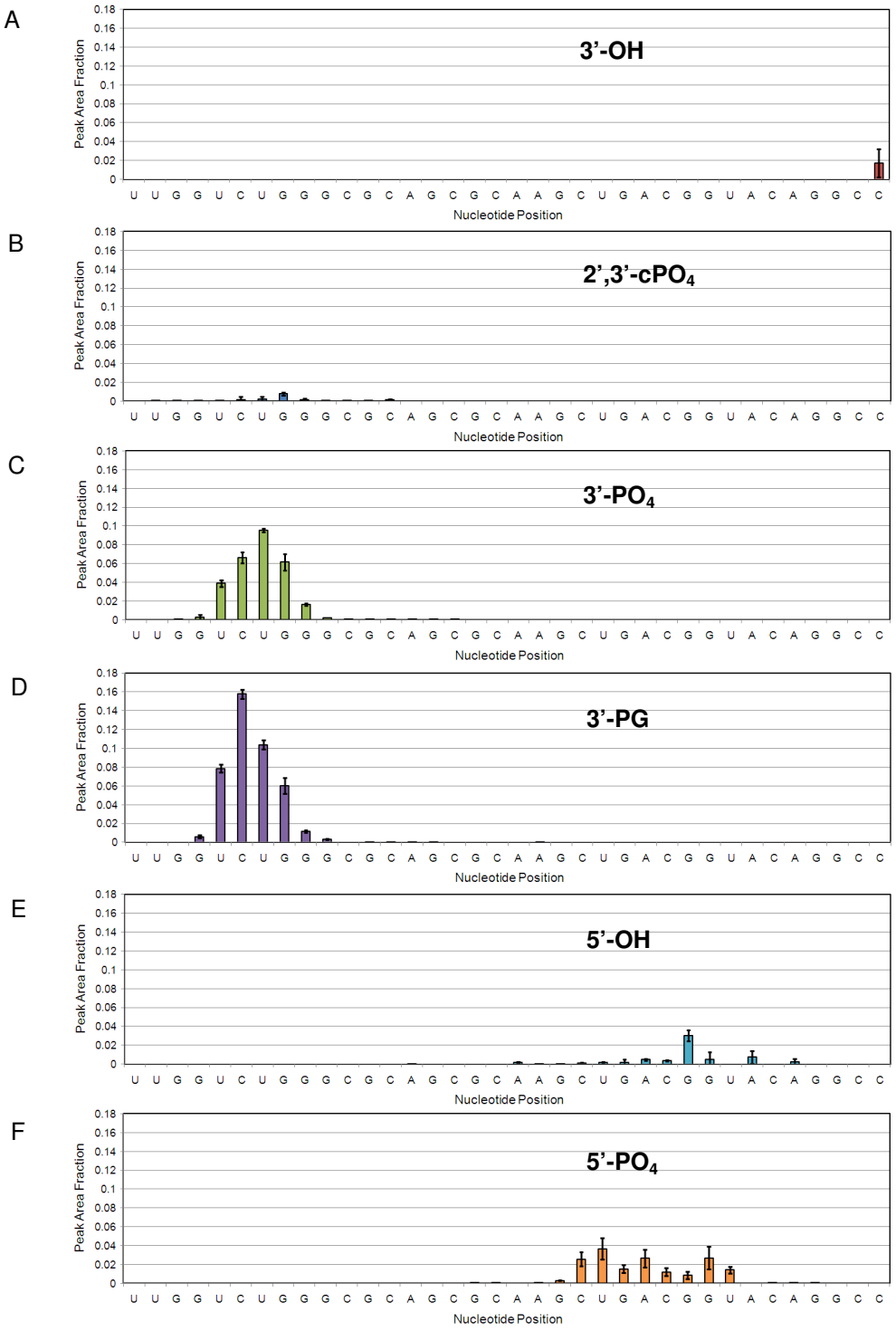

Figure SM37. Reproducibility of the MS data. The averages and standard deviations of peak area fractions are shown for each product (resulting from 3 separate reactions), for MS scans following the completion of reactions of 10 μM Fl-RRE RNA, 10 μM Fe-EDTA-Rev, 1 mM H_2O_2, and 1 mM ascorbate. The overhangs shown are: (A) 3'-OH, (B) 2',3'-cPO$_4$, (C) 3'-PO$_4$, (D) 3'-PG, (E) 5'-OH, (F) 5'-PO$_4$.

Base-Dependence of Oxidative Cleavage

At this Base	Relative Frequency of Oxidative Cleavage, Normalized to Account for Number of Base Positions (data obtained from sums of peak area fractions for preceeding 3'-PO_4 and 3'-PG, and succeeding 5'-PO_4)	Number of Positions in Fl-RRE RNA
A	3 ± 4 %	6
G	37 ± 17 %	14
U	41 ± 13 %	6
C	18 ± 8 %	10

Base-Dependence of 2'-OH-Mediated Transesterification

After this Base	Relative Frequency of 2'-OH-Mediated Transesterification, Normalized to Account for Number of Base Positions (data obtained from sums of peak area fractions for succeeding 2',3'-cPO_4)	Number of Positions in Fl-RRE RNA
A	1 ± 2 %	6
G	40 ± 30 %	14
U	40 ± 30 %	6
C	20 ± 30 %	10

Before this Base	Relative Frequency of 2'-OH-Mediated Transesterification, Normalized to Account for Number of Base Positions (data obtained from sums of peak area fractions for preceding 2',3'-cPO_4 fractions)	Number of Positions in Fl-RRE RNA
A	10 ± 20 %	6
G	50 ± 30 %	14
U	10 ± 20 %	6
C	20 ± 30 %	10

Table SM5. The base-dependence of RNA cleavage was analyzed separately for oxidative and endonucleolytic pathways, using extent of reaction MS data (after 1hr incubations), averaged from all reactions of 10 µM Fl-RRE RNA, 10 µM M-chelate-Rev, 1 mM H_2O_2, and 1 mM ascorbate. The data show that *oxidative* cleavage occurred least extensively at adenosine (A) positions. The 2'-OH-mediated *transesterification* reactions showed no statistically relevant dependence on the identity of the base preceding or succeeding the phosphate involved in cleavage, except that relatively few transesterifications occurred following (immediately 3' of) adenosine. However, it remains unclear whether the apparent base-dependences are either due to the intrinsic reactivity at specific bases or simply skewed by the positioning of the bases relative to the positions of the catalytic metal centers of bound M-chelate-Rev complexes. All cleavage data shown here are percentages based on the sums of cleavage products corresponding to each position in the RNA sequence (data separated by base) and were first normalized to account for the number of occurrences of each base (so that the number of occurences of a base does not systematically skew the data). Oxidative cleavage data were weighted after normalization based on the sums of the extents of cleavage (due to large variability in extents of oxidative cleavage among catalysts), so that reactions with more overall oxidative cleavage are weighted more.

Metal Ion	Coordination Number	Ionic Radius (Å)[a]	Average Total Rate of Cleavage for M-chelate-Rev Complexes Containing the Listed Transition Metal Ion (nM/min)	
			Oxidative Cleavage Products	Transesterification Products
Fe^{2+}	6 (high spin)	0.92	323.5	5.9
Co^{2+}	6 (high spin)	0.89	5.6	2.1
Ni^{2+}	6	0.83	3.7	1.5
Cu^{2+}	6	0.87	229.0	16.5

Table SM6. No general correlation was observed between the RNA-cleavage reactivity and the ionic radius of the transition metal contained within the M-chelate-Rev complexes. Rather, the rates were affected by complex combinations of the metal chelates' electronic parameters, reduction potential, degree of coordination unsaturation, geometry, nature of the ROS produced at each metal center, and possibly other parameters. The rates listed are the averages for each metal ion of the rates obtained from reactions of 10 µM Fl-RRE RNA, 10 µM M-chelate-Rev, 1 mM H_2O_2, and 1 mM ascorbate. The oxidative rates shown here were obtained from the sums of rates of formation of oxidative cleavage products (fragments containing nascent 3'-PO_4, 3'-PG, and 5'-PO_4 overhangs); transesterification rates were obtained from the sums of rates of formation of fragments containing nascent 2',3'-cPO_4 and 5'-OH overhangs. [a]Huheey, Keiter, and Keiter. Inorganic Chemistry: Principals of Structure and Reactivity (2000).[4]

SM REFERENCES

1. J. C. Joyner and J. A. Cowan, *J. Am. Chem. Soc.*, 2011, **133**, 9912-9922.
2. J. C. Joyner, K. Keuper and J. A. Cowan, *Nucl. Acids Res.*, 2012, **DOI: 10.1093/nar/gks811**.
3. K. A. Lacourciere, J. T. Stivers and J. P. Marino, *Biochemistry*, 2000, **39**, 5630-5641.
4. J. Huheey, E. Keiter and R. Keiter, *Inorganic Chemistry: Principles of Structure and Reactivity*, Pearson Education, Inc., 2000.